Tectonics®

RESEARCH ARTICLE
10.1029/2024TC008335

New Insights Into Active Tectonics and Landscape Evolution of the Northernmost Chilean Central Depression

A. Vega-Ruiz[1,2], P. Victor[1], K. Reicherter[3], A. Binnie[4], L. Evenstar[5], G. González[6], and S. A. Binnie[4]

[1]Deutsches GeoForschungsZentrum Potsdam, Potsdam, Germany, [2]Institute for Geological Sciences, Freie Universität Berlin, Berlin, Germany, [3]Neotectonics and Natural Hazards, RWTH Aachen University, Aachen, Germany, [4]Institute of Geology and Mineralogy, University of Cologne, Cologne, Germany, [5]School of Geography, Earth and Environmental Sciences, University of Plymouth, Plymouth, UK, [6]National Research Center for Integrated Natural Disaster Management, Departamento de Ciencias Geológicas, Universidad Católica del Norte, Antofagasta, Chile

Key Points:

- Quaternary reactivation of faults in the Atacama Desert is often overlooked due to low sedimentation rates and the lack of suitable stratigraphic markers
- We present an integrated geomorphic mapping approach to detect multi-scale Late Cenozoic-Quaternary faults concealed beneath arid alluvial plains
- These faults pose a source of seismic hazard that needs further dating of geomorphic markers and paleoseismological investigations

Supporting Information:

Supporting Information may be found in the online version of this article.

Correspondence to:

A. Vega-Ruiz,
vegaruiz@gfz-potsdam.de

Citation:

Vega-Ruiz, A., Victor, P., Reicherter, K., Binnie, A., Evenstar, L., González, G., & Binnie, S. A. (2025). New insights into active tectonics and landscape evolution of the northernmost Chilean central depression. *Tectonics*, *44*, e2024TC008335. https://doi.org/10.1029/2024TC008335

Received 14 MAR 2024
Accepted 3 DEC 2024

Abstract Active deformation and landscape evolution in North Chilean forearc involve multiscale tectonic processes, such as crustal thickening causing orogenic-scale uplift and faulting modulating the mountain-front landscape. In the Central Depression, faults redirecting Quaternary drainages are poorly understood due to their subtle surface expressions and limited structural data acquisition. To address this, we combined remote-sensing analysis of high-resolution DEMs, satellite and UAV imagery, new geomorphic mapping, structural data, and morphometric analysis with available surface age dating to identify and give temporal constraints on previously unmapped faults impacting drainages across this region. Our findings reveal the reactivation of east-vergent NNW-SSE reverse to transpressive and NW-SE strike-slip faults over approximately 100 km of latitude. Faults movement can be summarized into two main stages (a) A Late Miocene-Pliocene stage, dominated by east-vergent reverse faults inverting the Andean piedmont in the northern study area. (b) A Pliocene-Quaternary stage, characterized by transpressive activity of these east-vergent faults extending southward, alongside structures of the West Vergent Thrust System. The tectonic evolution of the east-vergent structures relates to the ongoing deformation of the coastal forearc, encroaching into the Central Depression. Minimum vertical and strike-slip displacement rates since the Quaternary are 12 m/Ma and 90 m/Ma, respectively, with the potential for higher rates depending on the onset of displacement. Drainage pattern modification, driven by incremental vertical displacement rates, provides insights to qualitatively evaluate individual fault activity rates. Numerous recently detected structures represent previously unknown sources of seismic hazard, requiring further dating of geomorphic markers and high-resolution monitoring.

Plain Language Summary The active deformation of the Northern Chile forearc involves the interplay of multiple complex tectonic processes, including fault structures, which are a significant source of seismic hazard. However, the role of faults in the deformation of the Central Depression and the timing of their activity remain unclear. Using advanced imaging techniques, geomorphic analysis, and field data, we identified previously unmapped, slow-moving faults affecting the Central Depression over approximately 100 km. A significant influence on drainage pathways was exerted by these structures from the Late Miocene to the Quaternary periods, primarily by inverting the Andean piedmont. We propose that these subtle structures are coupled with the tectonic evolution of the coastal region. This study provides a more complete understanding of the landscape evolution of the region and advises the inclusion of this structure in future seismic hazard assessments.

1. Introduction

Detecting and quantifying geomorphic evidence of Quaternary tectonic deformation is crucial for understanding active tectonics (Bullard & Lettis, 1993; De Pascale, 2021; Lettis et al., 1997) and the landscape evolution of a region (Medina-Cascales et al., 2021; Merritts & Vincent, 1989; Ritter et al., 2018). Active faults with slow displacement rates (<3 mm/a, Arrowsmith et al., 2017) are particularly challenging to detect and pose complex seismic hazard (Landgraf et al., 2017). These faults often have poor geomorphic expression, being blind or buried under undeformed sedimentary plains (e.g., Ishiyama et al., 2013; Maesano et al., 2015) and can remain unnoticed until generating moderate to major shallow earthquakes (Mw 5–7 with hypocenters <10 km depth) (e.g., Krüger et al., 2017; Nicol et al., 2018; Zhang, 2013). Despite low displacement rates, the interplay of the activity of these

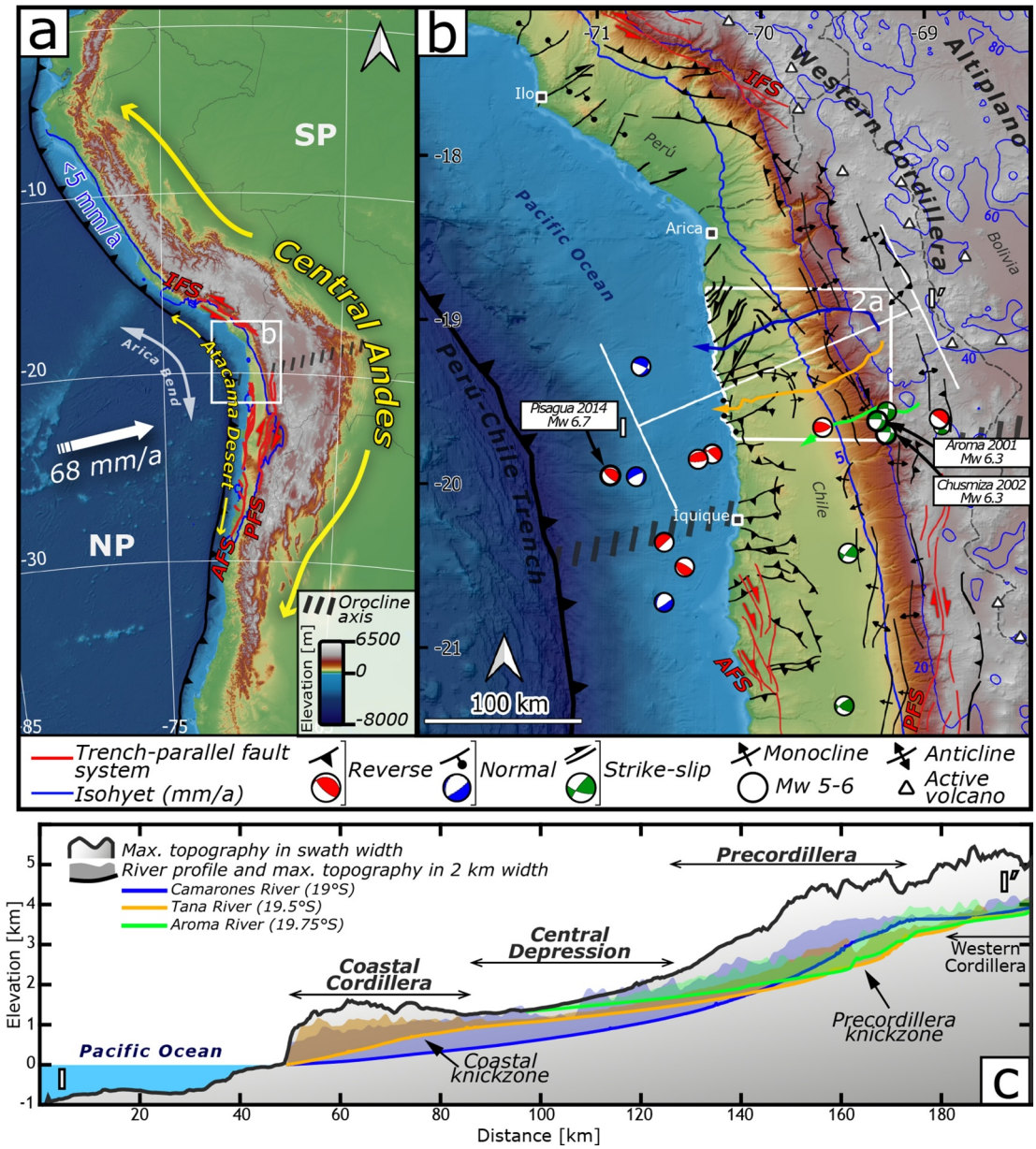

Figure 1. Climatic and tectonic setting of the study area. (a) Simplified setting of the Central Andes. Convergence vector from Norabuena et al. (1998). AFS = Atacama Fault System; IFS = Incapuquio Fault System; NP = Nazca Plate; PFS = Precordillera Fault System; SA = South American Plate. (b) Morphotectonic setting of the Central Andean forearc along the Arica Bend and recent seismicity moment tensor solutions. (c) Physiographic elements of the study area and disequilibrium (knickzones) along longitudinal profiles of trunk rivers. Faults from (Allmendinger & González, 2010; Audin et al., 2006; Benavente et al., 2017; Blanco & Tomilson, 2013; García et al., 2004, 2013; García & Fuentes, 2012; Habel et al., 2023; Morandé et al., 2015; Valenzuela et al., 2014). Upper plate focal mechanisms (<30 km depth) from (Farías et al., 2005; Herrera et al., 2021). Elevation data from GEBCO Bathymetric Compilation Group 2022. Isohyets from CHELSA global climate model (Karger et al., 2017, 2018).

faults and climate in desertic regions can leave a subtle yet detectable imprint on landscapes over Quaternary time scales (Pedrera et al., 2009; Pérez-Peña et al., 2010). Here, even minimal deformation and uplift rates (m to tens of m/Ma) can outpace erosion and deposition, leading to the long-term preservation of tectonic landforms (e.g., Audin et al., 2003; Whitney & Hengesh, 2015).

The Central Depression in Northernmost Chile is an arid to hyperarid region, considered tectonically stable since the Late Cenozoic (Jordan et al., 2010; Mortimer & Rendic, 1975; Nester & Jordan, 2012) (Figure 1a). Most fault structures in this region are blind and form gentle monoclines (García et al., 2004, 2013; García & Fuentes, 2012).

Only a few faults are recognized as potentially active during the Quaternary (Allmendinger & González, 2010; Carrizo et al., 2008; Maldonado et al., 2021; Santibáñez et al., 2019) and shallow upper plate seismicity (<20 km depth) is sparse (Sippl et al., 2023) (Figure 1b). A detailed geomorphological analysis and cosmogenic age dating of abandonment surfaces and fluvial deposits of windgaps at Pampa de Tana (ca. 19.5°S) indicate low Quaternary tectonic uplift rates of the pediplain above these blind structures (ca. 12 m/Ma, Binnie et al., 2020). Despite these findings, active faulting in the Central Depression remains understudied and poorly understood.

In this paper, we developed a detailed geomorphic mapping approach that enables the detection of subtle, slow-displacement Quaternary fault structures in desertic regions. This study was conducted in the Atacama Desert in northern Chile, between 18.75°S and 19.85°S (Figures 1 and 2). Here, close to the Orocline Bend (Arica Bend, Figure 1), the forearc exhibits a complex tectonic setting and has been struck by some of the largest instrumental upper plate earthquakes, including the Mw 5.9 Chusmiza in January 2002 (Farías et al., 2005), Mw 6.7 Pisagua in March 2014 (González et al., 2015), and the Mw. 6.3 Aroma in July 2001 (Legrand et al., 2007). The low Quaternary sedimentation rates (<2.1 m/Ma, Jungers et al., 2013) and erosion rates (<1.5 m/Ma, Placzek et al., 2014), combined with the absence of vegetation cover, provide ideal conditions for remote sensing analysis of geomorphic markers down to the size of 1 m. The region hosts a series of deeply incised canyons (hundreds of meters, Figure 1c), which enables the cross-checking of fault zones beneath deformed alluvial surfaces and displaced streams detected through remote sensing. These attributes make the study area an ideal site for detailed geomorphic mapping and ground-truthing. Our approach combines geomorphic mapping using remote sensing analysis of aerial imagery (Digital Globe, Bing, UAV) and DEMs at various resolutions: regional (TerraSar-X, 12.5 m/px), local high-resolution (SPOT-6, 2 m/px), and very high-resolution (UAV, 0.1–1.15 m/px). We supplemented this with a drainage network analysis (Whittaker, 2012; Wobus et al., 2006) using FABDEM Copernicus elevation (McMichael et al., 2022) and CHELSA precipitation (Karger et al., 2017, 2018) data sets (both 30 m/px) to identify fault-related disequilibrium in trunk rivers. New detailed structural data and field observations were collected to validate mapped structures and geomorphic markers, and thus to estimate surface offsets and along-strike displacements. By integrating these results with published age data, we calculated vertical and along-strike displacement rates for newly detected structures and evaluated fault-driven uplift and river disequilibriums.

2. Regional Background

2.1. Tectonostratigraphic Setting

The Central Andean forearc in northernmost Chile is part of the active Nazca-South America subduction margin, where the current convergence occurs at an azimuth of N78°E and rates of ca. 68 mm/a (Norabuena et al., 1998) (Figure 1a). This region comprises four latitudinal morphotectonic units from west to east (Figures 1b and 1c): (a) Coastal Cordillera, (b) Central Depression, (c) Precordillera, and (d) Western Cordillera. The first three units are also referred as the Atacama Bench, described as an uplifted regional-scale piedmont shaped by the Andean uplift and the aridity of the Atacama Desert (Armijo et al., 2015).

The Coastal Cordillera is a coastal mountain range with an average elevation of about 1,200 m.a.s.l. and represents a former and eroded Late Jurassic-Early Cretaceous volcanic arc (Scheuber & Reutter, 1992). It is deformed by the ca. 1,000 km long, trench-parallel Atacama Fault System (Figures 1a and 1b) and contains Oligocene-Pliocene intramountain basins (González et al., 2003; Mortimer et al., 1974). The boundary between the Coastal Cordillera and the Central Depression is often characterized as extensional (Buddin et al., 1993; Hartley et al., 2005).

The Central Depression is a ca. 40 km wide, N-S oriented forearc basin. Cenozoic continental and volcanic deposits, primarily sourced from the Western Cordillera (Armijo et al., 2015), unconformably overlie a Mesozoic substratum on an erosive surface (Choja pediplain, Galli-Olivier, 1967). The sedimentary cover exceeds 2,000 m in most areas (García et al., 2017) and is well constrained in the study area by the Tana-1A well (Gallardo, 1962) (Figure 2a). This well shows 432 m of Oligocene to Quaternary deposits, including the Azapa (Oligocene-Lower Miocene) and El Diablo Formations (19–8.3 Ma) (García et al., 2013), and Pliocene fluvial-lacustrine deposits (Evenstar et al., 2017; Kirk-Lawlor et al., 2013). Younger erosional horizons within the Cenozoic units record stages of the Andean uplift (e.g., Armijo et al., 2015; Mortimer & Rendic, 1975; Muñoz-Farías et al., 2023). The top of the Central Depression aligns with the Pacific Paleosurface, a regional pediplain extending over 1,200 km across northern Chile and southern Perú. This surface comprises several well-dated Late Cenozoic to Quaternary

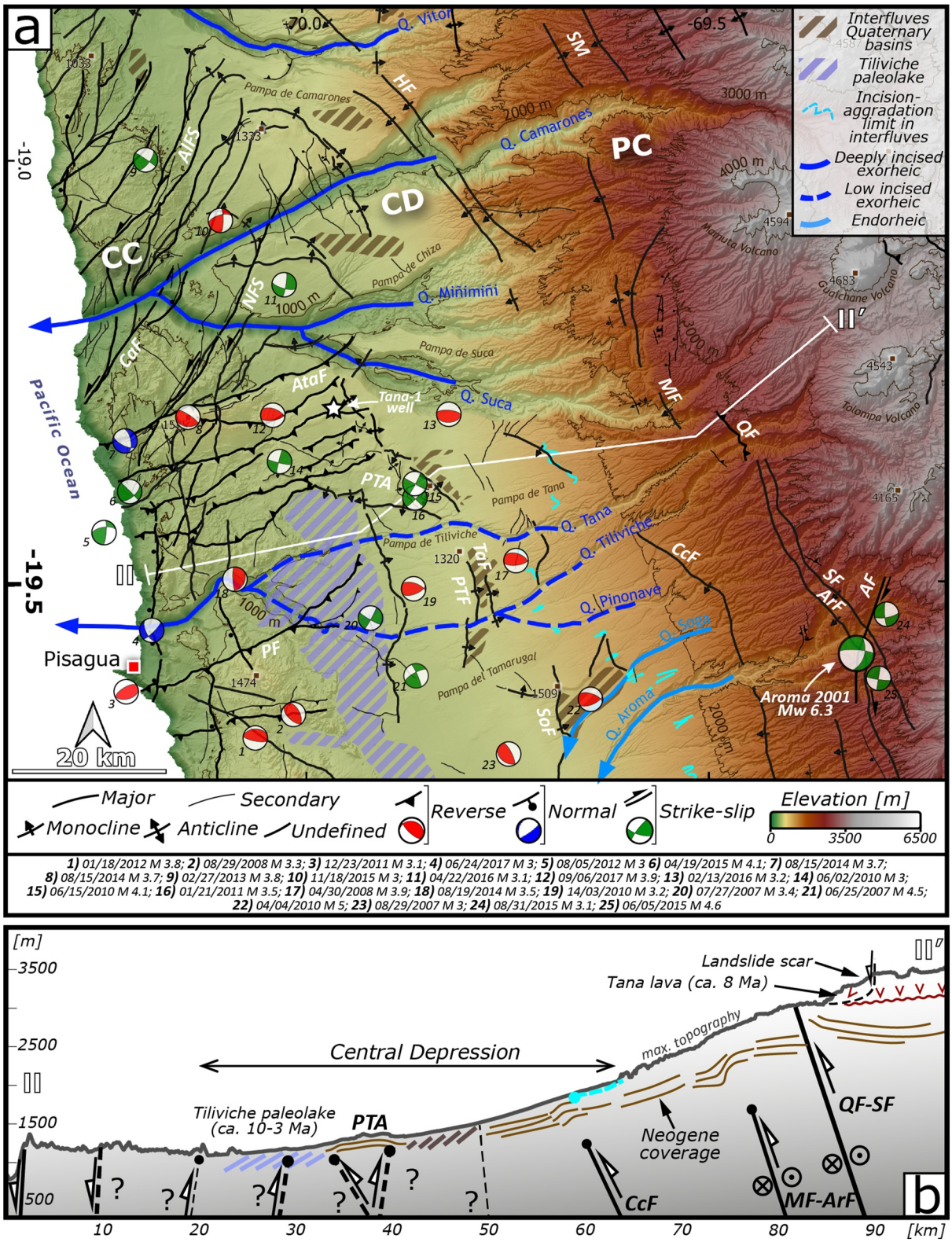
a
Interfluves Quaternary basins
Tiliviche paleolake
Incision-aggradation limit in interfluves
Deeply incised exorheic
Low incised exorheic
Endorheic
Q. Vitor
Q. Camarones
Q. Miniñiri
Q. Suca
Q. Tana
Q. Tiliviche
Q. Pinonave
Q. Saga
Q. Aroma
Pampa de Camarones
Pampa de Chiza
Pampa de Suca
Pampa de Tana
Pampa de Tiliviche
Pampa del Tamarugal
PC
CD
CC
Pacific Ocean
Pisagua
Tana-1 well
Aroma 2001 Mw 6.3
Mamuta Volcano
Guallatiri Volcano
Tolompa Volcano
HF
SM
AIFS
NFS
CaF
AtaF
PTA
PTF
TaF
PF
SoF
MF
QF
CcF
SF
ArF
AF
20 km
-69.5
-70.0
-19.0
-19.5
Major
Secondary
Monocline
Anticline
Undefined
Reverse
Normal
Strike-slip
Elevation [m]
0
3500
6500
1) 01/18/2012 M 3.8; 2) 08/29/2008 M 3.3; 3) 12/23/2011 M 3.1; 4) 06/24/2017 M 3; 5) 08/05/2012 M 3 6) 04/19/2015 M 4.1; 7) 08/15/2014 M 3.7;
8) 08/15/2014 M 3.7; 9) 02/27/2013 M 3.8; 10) 11/18/2015 M 3; 11) 04/22/2016 M 3.1; 12) 09/06/2017 M 3.9; 13) 02/13/2016 M 3.2; 14) 06/02/2010 M 3;
15) 06/15/2010 M 4.1; 16) 01/21/2011 M 3.5; 17) 04/30/2008 M 3.9; 18) 08/19/2014 M 3.5; 19) 14/03/2010 M 3.2; 20) 07/27/2007 M 3.4; 21) 06/25/2007 M 4.5;
22) 04/04/2010 M 5; 23) 08/29/2007 M 3; 24) 08/31/2015 M 3.1; 25) 06/05/2015 M 4.6
[m]
3500
2500
1500
500
Landslide scar
Tana lava (ca. 8 Ma)
max. topography
Central Depression
Tiliviche paleolake (ca. 10-3 Ma)
PTA
Neogene coverage
QF-SF
CcF
MF-ArF
b
10
20
30
40
50
60
70
80
90
[km]

Figure 2.

degradational and aggradational paleosurfaces (Evenstar et al., 2017, 2020). Cosmogenic ages in specific locations demonstrate that even younger fluvial systems have subsequently incised these paleosurfaces before becoming abandoned again (Binnie et al., 2020), evidencing a dynamically evolving landscape on a million-year timescale.

The Precordillera is a smooth, west-sloping mountain-front of the current volcanic arc, with Mid-Late Miocene lavas and volcanic edifices reaching elevations of ca. 4,700 m (Figure 2a). It is deformed by the ca. 600 km long, trench-parallel, and transpressive Precordillera Fault System (Reutter et al., 1991, 1996; Victor et al., 2004). West-vergent reverse faults deformed the Precordillera during the Late Oligocene-Late Miocene (Nester & Jordan, 2012; Victor et al., 2004), and possibly earlier during the Paleocene-Early Eocene (Habel et al., 2023). To the east, the Western Cordillera crowns the forearc with Pliocene-Recent stratovolcanoes covering a Mesozoic basement high (Armijo et al., 2015; Habel et al., 2023), exciding 5,000 m in elevation. A Neogene fault system of east-vergent reverse faults is suggested to control its eastern boundary to the Altiplano (Cortés et al., 2012; Farías et al., 2005) (Figure 1b).

From 20°S to 17°S, the Central Andes margin deflects from a N-S to a NW-SE strike, forming the Arica Bend (Comte et al., 2003; Madella et al., 2018) (Figure 1b). In this region, fault orientations deviate from the trench-parallel trend observed along Northern Chile in southern latitudes. The elevation of the Coastal Cordillera decreases rapidly from ca. 1,200 m.a.s.l at 20°S, and its topographic expression disappears north of 18.5°S. The Atacama Fault System can be followed onshore up to the same latitudes (ca. 20°S), with the NW-SE Salar Grande and Iquique Faults marking its northern tip (Figure 1b). To the north, instead, a system of seismically active ENE-WSW reverse faults (Allmendinger et al., 2005; González et al., 2015, 2021) and sinistral NE-SW strike-slip faults are present (Figures 1b and 2a). To the east, the boundary between the Coastal Cordillera and the Central Depression is diffuse. The reverse faults accommodate N-S along trench shortening driven by the interplay of the margin curvature and oblique subduction since Pliocene times (Allmendinger et al., 2005). Scarce but well-defined N-S normal faults near the coastal escarpment crosscut the reverse faults. One of the NE-SW striking faults, the Camarones Fault (Figure 2a), has been proven to be active in the Holocene (Niemeyer et al., 1984).

In the western Central Depression, NW-SE blind fault structures, such as the Pampa de Tana Anticline (PTA) (Figures 2a and 2b), have modified slow-incising alluvial channels (<3 m/Ma in the last 2 Ma) during the Pliocene and Quaternary, despite very low surface uplift rates (ca. 12 m/Ma, Binnie et al., 2020). Other structures in the area likely correspond to similar blind reverse faults (García et al., 2004, 2013; García & Fuentes, 2012). Moment tensor solutions of deep seismicity (>25 km depth) indicate strike-slip kinematics beneath the location of coastal NE-SW sinistral fault systems and these NW-SE blind faults (Herrera et al., 2021).

In the Precordillera, no clear trench-parallel master fault separates the arc from the forearc. Instead, NW-SE west-vergent reverse faults are present (Farías et al., 2005) (Figures 1b and 2a), which currently host strike-slip earthquakes (Legrand et al., 2007; Sippl et al., 2023) (Figures 1b and 2a). Similar faults are reported at the latitude of Arica (ca. 18.5°S) (Muñoz & Charrier, 1996) and Santiago cities (ca. 33.5°S) (Ammirati et al., 2019; Armijo et al., 2010; Riesner et al., 2017, 2018).

2.2. Climate, Erosion and Deposition Rates

The Central Andean forearc has been shaped under the predominantly hyperarid conditions of the Atacama Desert since at least the Middle Miocene (Alpers & Brimhall, 1988; Jordan et al., 2014; Sillitoe & McKee, 1996). This hyperaridity, coupled with an increasing topographic precipitation gradient (Figure 1b), is linked to the Middle Miocene onset of the Peru-Chile Oceanic Current and the Andean rain shadow effect (Houston & Hartley, 2003). Global climate fluctuations resulted in wetter, though still arid, phases across the forearc from the Miocene to the Pleistocene (Evenstar et al., 2009; Jordan et al., 2014; Zachos et al., 2001). A final regional hyperarid phase is generally agreed to have occurred around 2 Ma (Amundson et al., 2012; Jungers et al., 2013; Wang et al., 2015). Neogene pluvial phases left several aggradational surfaces in the

Figure 2. Summary of previously identified tectonic structures and geomorphic features within the study area. (a) Faults and overall drainage patterns across the forearc. Upper plate focal mechanism from Farías et al. (2005) and Herrera et al. (2021). Tiliviche paleolake extension from Kirk-Lawlor et al. (2013). AF = Aroma Fault; ArF = Aroma Flexure; AlFS = Alejo Fault System; AtaF = Atajaña Fault; CaF = Camarones Fault; CC = Coastal Cordillera; CcF = Calacala Flexure; CD = Central Depression; CF = Camiña Fault; HF = Humayani Flexure; MF = Moquella Flexure; NFS = Negrito Fault System; PC = Precordillera; PCA = Pampa de Camarones Anticline; PF = Pisagua Fault; PTA = Pampa de Tana Anticline; PTF = Pampa de Tiliviche Fault; QF = Quisagama Fault; SF = Soga Flexure; SM = Sucuna Monocline; SoF = Soga Fault; TaF = Tamarugal Fault. (b) Topographic swath profile of the study area and schematic main tectonic and sedimentary features.

Table 1
Classification of Drainage Networks Within the Study Area as Well as Analysis Type According to Their Characteristics

River classification		Basin area (km^2)	Bed type	Drainage pattern	Incision (m)	Flow activity	Headwaters location	Extraction method	Performed analysis
Trunk rivers	Vitor River Basin	2,262	Bedrock	Parallel, exorheic	Mid mean = 404 max = 670 min = 99	Active	Western Cordillera	Semiautomatic extraction from DEM with exclusion of interfluves ("pampas") channels	Longitudinal profiles, k_{snP}, knickpoints and paleo-profile projections
	Camarones River Basin	4,630		Sub-dendritic, exorheic	Very High mean = 640 max = 1,105 min = 32				
	Tana River Basin	4,487		Dendritic to subparallel, exorheic	High mean = 362 max = 1,032 min = 58 m				
	Soga River Basin	237	Bedrock to alluvial	Parallel, endorheic	Mid to Low mean = 186 max = 827 min = 6				
	Aroma River Basin	1,846	Bedrock	Dendritic to subparallel, endorheic	Mid mean = 381 max = 806 min = 24				
Alluvial channel in interfluves ("pampas")	Paleo-channels Quaternary channels	– –	Alluvial	Subparallel to parallel, endorheic	Low (<20 m)	Abandoned Sporadic	Precordillera	Mapping	As linear geomorphic markers for faulting

Central Depression and Precordillera. These are grouped into five generations based on regional geomorphologic characteristics and cosmogenic exposure ages (^{26}Al, ^{10}Be, ^{21}Ne in quartz; ^{3}He in pyroxene and amphibole): Surface 5 (ca. 20.2–18.4 Ma), Surface 4 (ca. 16.3–11 Ma), Surface 3 (7.8–6.8 Ma), Surface 2 (ca. 4.3–2.5 Ma), and Surface 1 (Quaternary) (Evenstar et al., 2017). These surfaces have been used as regional markers to constrain the Andean uplift (Evenstar et al., 2020).

Late Cenozoic and Quaternary erosion and deposition rates vary across the forearc but are generally very low, indicating slow or rarely operating surface processes. In the Coastal Cordillera, Late Cenozoic erosion rates are the lowest (<0.1 m/Ma, Dunai et al., 2005), with Quaternary rates ranging from 0.4 to 2.5 m/Ma (Kober et al., 2007; Placzek et al., 2014). Coastal claypan records indicate Late Quaternary deposition rates of <0.1 m/Ma (Diederich et al., 2020; Wennrich et al., 2024). Quaternary erosion rates in interfluves of the Central Depression and Precordillera range from 0.2 to 1.5 m/Ma (Placzek et al., 2014), and even lower in some regions (<0.1 m/Ma, Nishiizumi et al., 2005), while deposition rates are 2–2.1 m/Ma (Jungers et al., 2013).

2.3. Drainage Pattern and Its Evolution

Current drainages in the North Chilean forearc can be categorized into three distinct types (Binnie et al., 2020; Hoke et al., 2004; Mortimer, 1980): (a) trunk rivers in the canyons ("quebradas"), along with their tributaries, (b) perched active alluvial channels and (c) inactive alluvial channels, also referred to as paleochannels (Binnie et al., 2020; Ritter et al., 2018), both located within the remaining interfluves ("pampas") (Table 1). The study area contains three exhoreic trunk rivers (Vitor, Camarones, and Tana Rivers), which outlet into the Pacific Ocean, and two endorheic trunk rivers (Soga and Aroma Rivers), which outlet into the Central Depression.

The incision history of these trunk rivers is controlled by the interplay between the Andean uplift and variations in precipitation rates in the catchment areas (Coudurier-Curveur et al., 2015; García et al., 2011; Schildgen

et al., 2007). Deep incision of trunk rivers in Northern Chile began around 11 Ma in the Precordillera and between 6 and 3 Ma in the Central Depression (García et al., 2011; Hoke et al., 2007; Kirk-Lawlor et al., 2013). The longitudinal profiles of these rivers show distinct segments: a low-concavity, shallow-incised upstream segment across the Precordillera-Western Cordillera, bounded by a knickzone to a high-concavity and deeply incised downstream segment (Farías et al., 2005; Hoke et al., 2007; Mortimer, 1980) (Figure 1c). This disequilibrium in rivers profile is attributed to fault-induced surface uplift from ca. 30 to 10 Ma, followed to mid-crustal thickening under the High Andes in the last 10 Myr, causing about 1 km of surface uplift relative to the Central Depression (e.g., Hoke et al., 2007; Schildgen et al., 2007, 2009; Thouret et al., 2007). As a result, alluvial channels in the pampas were disconnected from major river catchments and remained perched. Current active perched drainages in the interfluves are fed by sporadic precipitation in the Precordillera (e.g., Bozkurt et al., 2016).

From ca. 19.5° toward the Arica Bend, trunk rivers are deeply incised across the Coastal Cordillera, flowing into the Pacific Ocean (Figures 1b and 1c & 2a). A second coastal knickzone is present in the Quebradas Tana and Tiliviche drainages (Figure 1c), where a paleolake/wetlands existed along the eastern margin of the Coastal Cordillera until the Early Pliocene (Figure 2) (Kirk-Lawlor et al., 2013). This second knickzone has been attributed to different factors. García et al. (2011) suggest it resulted from reduced precipitation in the Tana and Tiliviche catchments due to increasing aridity across the forearc, leading to a later (<6.4 Ma) and less intense incision compared to the Camarones River Basin in the north. Other authors argue that the knickzone reflects a threshold where coastal uplift rates have exceeded the river incision rates (Coudurier-Curveur et al., 2015; Kirk-Lawlor et al., 2013; Madella et al., 2018).

The proposed mechanisms for this coastal uplift vary. Armijo et al. (2015) and Coudurier-Curveur et al. (2015) attribute it to the westward widening of the Andean orogen, while Schildgen et al. (2009) link it to subduction zone processes with minor Andean widening influence. Madella et al. (2018) propose a negative feedback cycle, wherein reduced sediment infill in the subduction channel enhances interplate coupling, driving higher coastal uplift rates that impedes drainage to outlet into the Pacific Ocean. Kirk-Lawlor et al. (2013) offer a combined explanation involving both coastal retreat and uplift to account for the coastal knickzone, though they do not specify the precise underlying drivers of uplift.

3. Methods

3.1. High-Resolution Geomorphic Mapping

We developed a comprehensive Late Cenozoic to Quaternary fault database at a scale of 1:10,000 to identify previously undetected faults (Figure 2a). Building on existing active fault databases (Maldonado et al., 2021; Santibáñez et al., 2019), we refined and adapted these using the mapping procedures defined in Mittelstädt and Victor (2020). Our high-resolution mapping focused on the detection of fault scarps and folds by using geomorphic markers, such as drainage patterns indicating changes in slope gradient, displaced or deflected drainages, abandoned and deformed fluvial-alluvial surfaces (Holbrook & Schumm, 1999; Oskin et al., 2007), and shutter ridges (e.g., Densmore et al., 2007; Wang et al., 2014). We mapped fluvial-alluvial surfaces (Evenstar et al., 2017) and channels, including Quaternary ones, using surface coloration changes in optical satellite imagery (Bing Aerial, Digital Globe, SPOT-6) and aspect and roughness maps derived from the TerraSAR-X DEM (12.5 m/px). To emphasize tectonic landforms and small-scale topographic features, we generated Red Relief Image Maps (RRM) (Chiba et al., 2007) from this DEM (e.g., Benavente et al., 2022; Kondo et al., 2008). We used UAV-derived high-resolution orthophotos and DEMs obtained during fieldwork for key areas. Data acquisition involved planned horizontal flights with a DJI Phantom 4 UAV, flown at 130 m above ground level. A total of 4,129 photos were captured with 80% frontal and 70% lateral overlap, covering a total area of over 8 km^2. The imagery data set was processed using Metashape Pro Software following the workflow in Carbonneau and Dietrich (2017).

Tectonic cracks, caused by regional tectonic stresses (Loveless et al., 2005, 2009) and extensional bending in the hanging wall above reverse faults (e.g., Klinger et al., 2005), have been utilized to identify recent surface deformation in Northern Chile (González et al., 2008; Loveless et al., 2005, 2009). To complement our fault database, we developed a 1:2,500 scale fracture map, employing the same methods and basemaps as for fault mapping (Figure S1 in Supporting Information S1). Fractures were classified as tectonic based on their proximity to faults (<1 km) and azimuthal deviation (±30° from the fault strike) following González et al. (2008). We included non-tectonic fractures to document other active processes modifying the landscape, such as landslides,

which have been triggered by both megathrust (Crosta et al., 2014; Keefer & Moseley, 2004) and crustal earthquake-induced destabilization (Pinto et al., 2008).

Both faults and fractures were mapped using QGIS 3.16.5 (https://www.qgis.org). Details of the data sets are in Figure S2 and Table S1 in Supporting Information S1. Fieldwork for ground truthing was performed during two campaigns using FieldMove Clino© (Midland Valley, 2014) and a Freiberg structural compass for verification (Table S2 in Supporting Information S1).

3.2. Quantification of Vertical Displacement and Along-Strike Displacement Rates of Faults

To quantify the net vertical uplift caused by major folding and faulting detected through geomorphic mapping, we applied a 2D geometric approach using topographic swath profiles and structural data (Yang et al., 2015) (Figure 3a). We extracted 51 swath profiles (500–2,500 m wide) perpendicular to the strike of six major fault scarps along the western Central Depression. We used the TerraSAR-X DEM, which provides a high-resolution (vertical resolution <2 m) and homogeneous coverage across the study area (Table S3 and Figure S3 in Supporting Information S1).

We first quantified the mean of the vertical separation (VS) between the hanging wall and footwall best linear fits (Figure 3a). Since the coverage of exposure age samples is scattered and it is common to observe inheritance (pre-exposure) of clasts derived from older reworked paleosurfaces or fan material upstream (e.g., Binnie et al., 2020), we calculated displacement rates by using the youngest in situ age of the displaced paleosurface where available (Binnie et al., 2020; Evenstar et al., 2009, 2017) (Table S3 in Supporting Information S1). In regions lacking cosmogenic exposure age data, we used the minimum regional age of termination of sedimentation of the El Diablo Formation constrained by the overlying Tana Lava (ca. 8.3 Ma) (García et al., 2004; Naranjo & Paskoff, 1985). For comparative analysis, we calculated rates using both the oldest in situ cosmogenic exposure age or subsurface geologic markers of the displaced surface, and the minimum regional age of the surface suggested by Evenstar et al. (2017). Along-strike displacements were quantified based on the lateral displacement of offset Quaternary alluvial channels, using the approach of Zielke and Arrowsmith (2012) (Figure 3b and Table S4 in Supporting Information S1). The compilation of the available age data used for calculating the displacement rates is provided in Table 2 and Figure 7.

3.3. Drainage Analysis of Trunk Rivers

Rivers in Northern Chile and Southern Peru have been analyzed as bedrock rivers using Flint's (1974) stream power law (e.g., Abbühl et al., 2011; Coudurier-Curveur et al., 2015; Hoke et al., 2007). We calculated the longitudinal profiles of trunk rivers using TopoToolbox2 for MATLAB (Schwanghart & Scherler, 2014) in order to detect fault-related disequilibria. Drainage networks were extracted from the regional FABDEM Copernicus data set (30 m/px) (McMichael et al., 2022) with a minimum upslope area of $A = 5$ km^2. We applied a non-parametric regression algorithm for hydrological correction, using an optimal smoothing degree of $K = 2$ for a τ (quantile) $= 0.1$ based on visual inspection of results (Schwanghart & Scherler, 2017). We calculated the normalized steepness index with precipitation correction (k_{snP}) (Adams et al., 2020; Leonard et al., 2024) using an estimated best-fit reference concavity (θ_{ref}) value of 0.51 for the study area (Figure S4 in Supporting Information S1). This value is consistent with theoretical range of 0.3–0.6 and values expected for the study area (0.15–2.0, Hoke et al., 2007). Precipitation correction was performed using the CHELSA precipitation model (Karger et al., 2017, 2018), following Gelwick et al. (2024).

Knickpoints and knickzones are often found in river segments where k_{snP} values deviate, indicating possible tectonic forcing in regions with minimal spatial variations in rock erodibility (Kirby & Whipple, 2012). We extracted knickpoints using the semi-automated *knickpointfinder* algorithm (Schwanghart & Scherler, 2014) with a quantile tolerance range of 0.1–0.9 to filter outliers (Forte & Whipple, 2019; Schwanghart & Scherler, 2017). The nature of knickpoints, whether tectonic (fault-related or regional), minor, or non-tectonic, was verified based on k_{snP} values per lithology, slope-break morphology of knickpoints indicative of tectonics in χ-elevation plots, and their proximity to lithological boundaries, active faults, and landslides observed in geological maps and satellite imagery data sets (Figure S5 and Table S5 in Supporting Information S1) (e.g., Clementucci, Ballato, Siame, Faccenna, et al., 2023; Clementucci, Ballato, Siame, Fox, et al., 2023; Clementucci et al., 2024; Kaveh-Firouz et al., 2024).

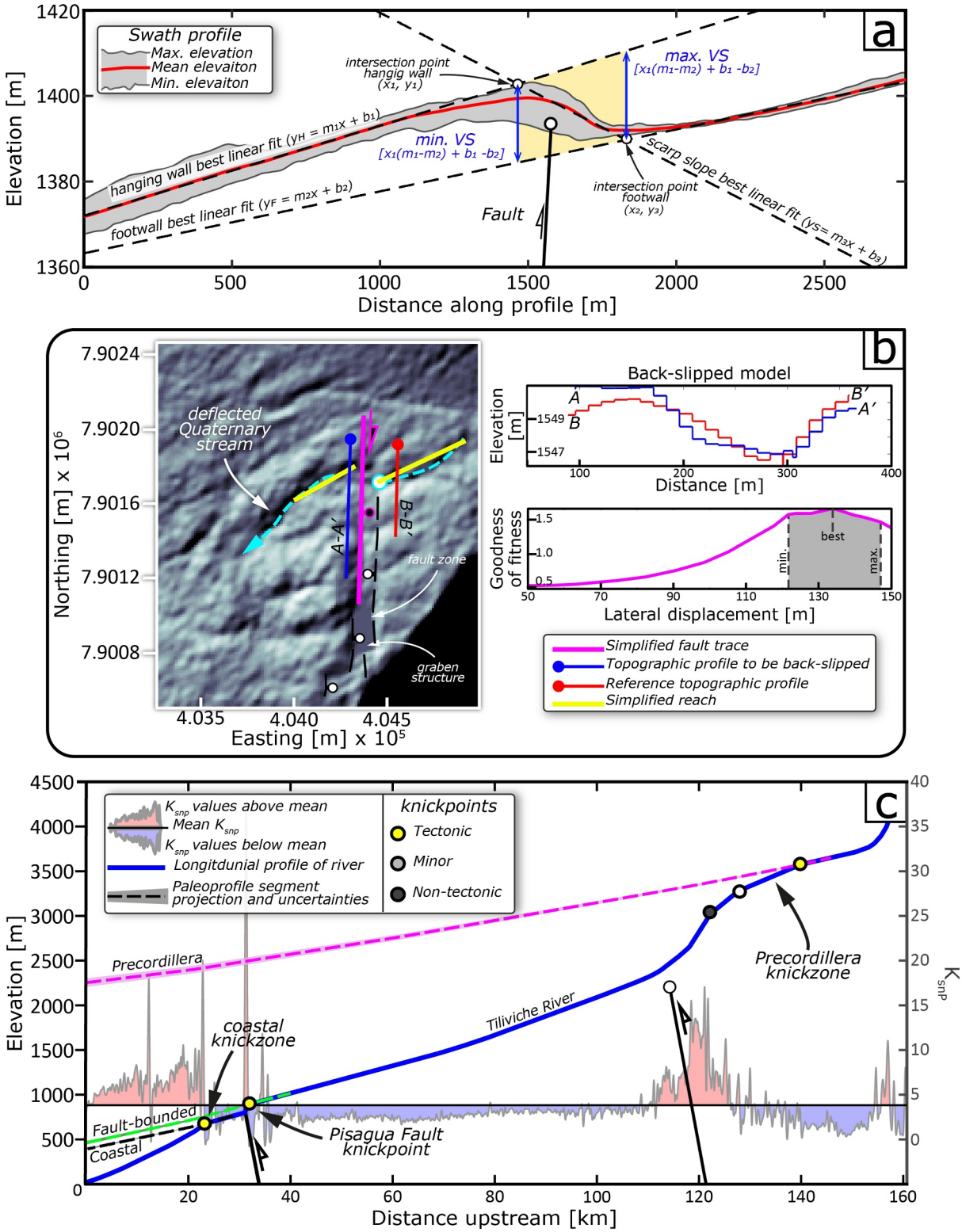

Figure 3. Examples of analysis to quantify net vertical displacement, along-strike displacement, and tectonic relief fault. (a) Swath profile across the scarp of the Pampa Tiliviche Fault and geometric elements used for surface uplift rate quantification (Yang et al., 2015). VS = Vertical Separation. (b) Deflected alluvial channel and quantification of mean along-strike displacement shown in LaDiCaoz interface (Zielke & Arrowsmith, 2012). (c) Longitudinal profile of the Tiliviche River with k_{snP} anomalies, knickpoint bounded segments, and paleo-profile projections used for tectonic relief quantification.

Table 2
Compilation of Available Age Data Used for the Quantification of Displacement Rates

Interfluve	Lat (°)	Long (°)	Sampled material	Dating method	Age (Ma)	Error (±Ma)	Reference	Used as
Pampa de Camarones	−69.989	−19.022	Tuff	K-Ar in biotite	**15.69**	**0.7**	García et al. (2004)	**Subsurface marker**
			Surface 5		**18.41**	**0.25**	Evenstar et al. (2017)	**Minimum regional age**
Pampa de Tana	−68.880	−19.397	Boulder	^{3}He in pyroxene	11.1	0.3	Evenstar et al. (2017)	
	−68.880	−19.397	Boulder	^{3}He in pyroxene	16.6	0.4		
	−68.880	−19.397	Boulder	^{3}He in pyroxene	20.2	0.7		
			Mean age		**15.7**	**0.5**		**Oldest in situ age**
	−69.839	−19.386	Cobble	^{26}Al in quartz	2.25	1	Binnie et al. (2020)	
	−69.839	−19.386	Cobble	^{21}Ne in quartz	2.63	0.29		
	−69.839	−19.386	Cobble	^{21}Ne in quartz	4.93	0.69		
			Mean Age		**3.27**	**0.8**		**Youngest in situ age**
			Surface 5		**18.41**	**0.25**	Evenstar et al. (2017)	**Minimum regional age**
Pampa de Tiliviche	−68.808	−19.522	Boulder	^{3}He in pyroxene	**3.19**	**0.4**	Evenstar et al. (2017)	**Youngest in situ age**
	−68.808	−19.522	Boulder	^{3}He in pyroxene	**16.3**	**0.4**	Evenstar et al. (2017)	**Oldest in situ age**
			Surface 5		**18.41**	**0.25**	Evenstar et al. (2017)	**Minimum regional age**
Pampa del Tamarugal	−69.629	−19.706	Boulder	^{3}He in amphibole	6.8	0.0	Evenstar et al. (2009)	
	−69.629	−19.706	Boulder	^{3}He in amphibole	7.3	0.0		
			Mean Age		**7.05**	**0.0**		**Youngest in situ age**
			Surface 4		**11**	**0.0**	Evenstar et al. (2017)	**Minimum regional age**

Note. The numerical values in bold letters are the ages considered for this study, coming from the average of several dated material or directly from a dated marker.

We projected paleo-profiles of river segments upstream from the newly detected tectonic knickpoints and knickzones (Figure 3c). This allowed us to estimate the possible gained relief due to faulting between current river outlet elevations and those of the paleo-profile projections (e.g., Clark et al., 2005; Gallen et al., 2013). We applied a correction of −1,000 m to the paleo-profile projections of the Precordillera segment of exorheic drainages (Hoke et al., 2007). Paleo-profile projection was carried out using the Topographic Analysis Kit for TopoToolbox2 (Forte & Whipple, 2019) (Figure S6 and Table S6 in Supporting Information S1).

4. Results

4.1. Fault Database and Geomorphic and Structural Evidence for Fault Reactivation

The resulting fault database of the study area (Figure 4) includes a total of 1,092 fault structures. We found 82 new major structures over the 110 previously mapped and 734 new secondary structures over the 166 previously documented. Additionally, the database includes 11,277 tectonic fractures, mainly found along reverse fault scarps, and 1,363 non-tectonic fractures, mainly related to landslide scars. The length of completeness of our database, that is, the smallest features comprehensively mapped, is 2 km for faults and 100 m for fractures. A detailed description of the fault database and the database as downloadable GIS or.kmz files are available in Supporting Information S2.

The Coastal Cordillera is characterized by long (>40 km) N10-20°E striking, sub-vertical sinistral faults and N35-40°E reverse faults (Figures 4 and S7a in Supporting Information S1). Tectonic fractures are mostly found along the hanging walls of the prominent reverse faults, particularly the Atajaña and Pisagua Faults, consistent with their reverse kinematics (Figures 4 and S7b in Supporting Information S1). The dominant orientations of these fractures are N80°W and N10°E, with an average length of 200 m (Figures 4a and 4b). In the Precordillera, subparallel N10-15°W west-facing monoclines are often accompanied by N-S oblique normal faults along their hinges (Figures 4a and 4b).

The Central Depression hosts the majority of the newly identified structures, including 556 faults of <5 km in length (Figures 4 and S7a in Supporting Information S1). Many of these are NNE-SSW oriented, secondary oblique extensional faults forming small en echelon graben structures atop NW-SE west-facing monoclines and east-facing monoclines (Figures 5 and 6). The east-facing monoclines are often highlighted by fracture systems in

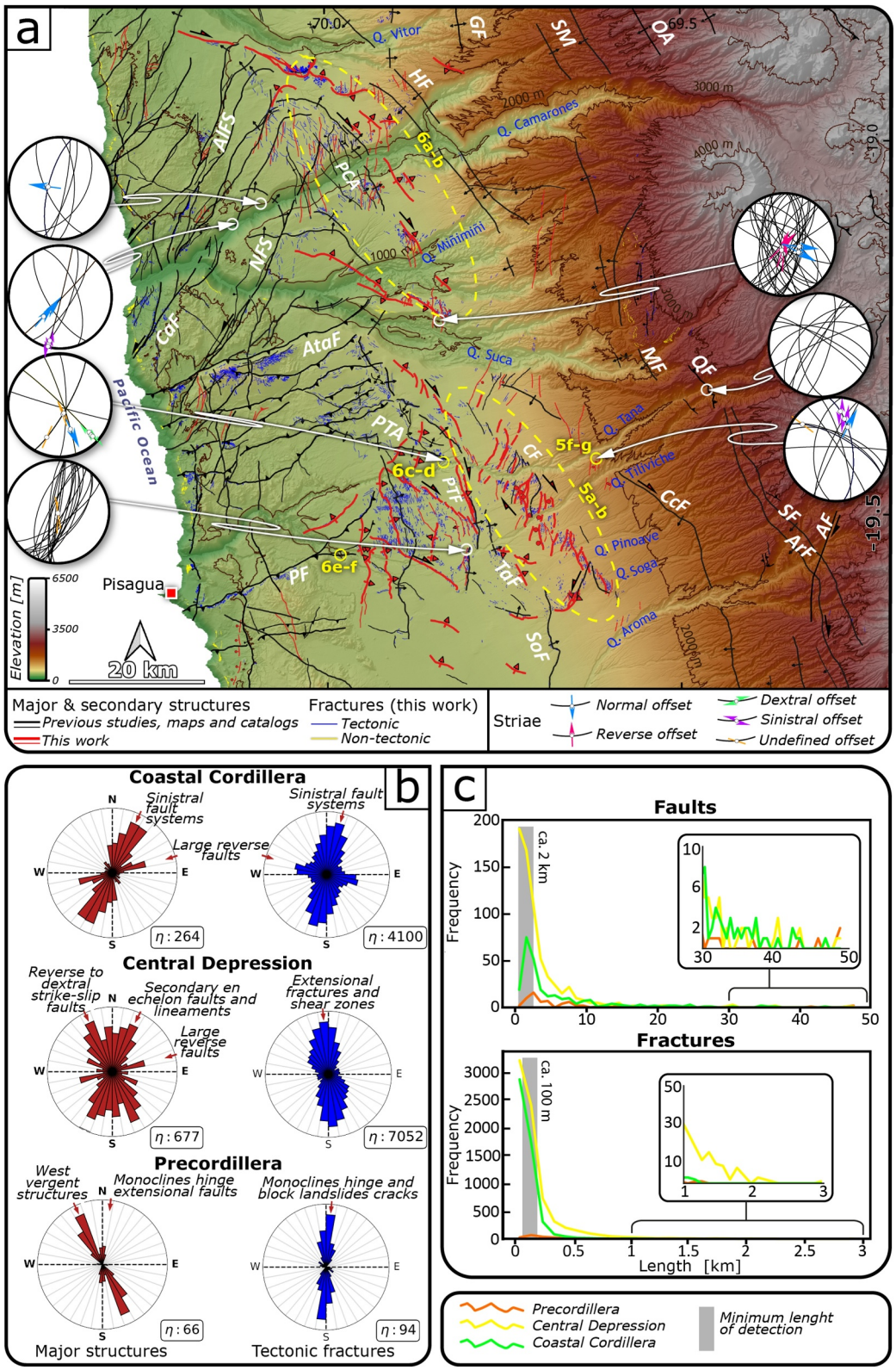
a
Q. Vitor
GF
SM
OA
HF
Q. Camarones
AIFS
6a-b
PCA
NFS
Q. Miniñini
CdF
AtaF
Q. Suca
MF
QF
Pacific Ocean
PTA
6c-d
PTF
Q. Tana
5f-g
CF
Q. Tiliviche
5a-b
CCF
Q. Pinoave
Q. Soga
SF
ArF
AF
PF
6e-f
IdF
SoF
Q. Aroma
Pisagua
Elevation [m]
6500
3500
0
20 km
-19.5
Major & secondary structures
Previous studies, maps and catalogs
This work
Fractures (this work)
Tectonic
Non-tectonic
Striae
Normal offset
Reverse offset
Dextral offset
Sinistral offset
Undefined offset
b
Coastal Cordillera
Sinistral fault systems
Large reverse faults
η: 264
Sinistral fault systems
η: 4100
Central Depression
Reverse to dextral strike-slip faults
Secondary en echelon faults and lineaments
Large reverse faults
η: 677
Extensional fractures and shear zones
η: 7052
Precordillera
West vergent structures
Monoclines hinge extensional faults
η: 66
Monoclines hinge and block landslides cracks
η: 94
Major structures
Tectonic fractures
c
Faults
Frequency
ca. 2 km
Fractures
ca. 100 m
Length [km]
Precordillera
Central Depression
Coastal Cordillera
Minimum lenght of detection

Figure 4.

the hanging wall, especially in the area of the Pampa de Camarones and Pampa de Tiliviche interfluves (Figures 4a and S7b in Supporting Information S1). Tectonic fractures in this region are ca. 150 m long with a N-S orientation associated with the secondary extensional faults (Figure 4b).

The Camiña Fault is a key example of a newly detected west-vergent structure in the Central Depression (Figure 4a). The Camiña Fault is a subtle NNW-SSE striking monocline located between Quebrada Tana and Quebrada Aroma (Figure 5). Between Quebrada Tana and Pinonave, the monocline features an array of prominent N30°W-N35°E striking sigmoidal fault scarps of >7 km long. These scarp faults deform the aggradational Surface 4 and form small pull-apart basins, each less than <1 km^2, which contain remnants of Surfaces 3-2. Quaternary alluvial channels show right-lateral deflections averaging 43 m along NNW-SSE segments of the sigmoidal faults and left-laterally deflections averaging 120 m along the NNE-SSW segments. The left-lateral deflection increases as the faults approach a NE-SW strike. This overall complex geometrical arrangement is indicative of a strike-slip dextral duplex (Figure 5b). Ground truthing revealed that this dextral duplex is related to sub-vertical subsidiary faults deforming Upper Miocene rocks of the El Diablo Formation (Figure 5e). Other faults along the Calacala Flexure moncoline hinge (Figure 4a) were confirmed to be normal to transtensional faults deforming the same stratigraphy (Figures 5f and 5g). This suggests an oblique component in the latest activity of the faults beneath these flexures.

Between Quebrada Pinonave and Quebrada Aroma, secondary structures correspond to numerous N15°E and N15°W subparallel fault scarps. The subtle (<1 m high) scarps, often visible as whitish gypsum-rich, decametric-wide features in satellite imagery and the field (Figures S8a and S8b in Supporting Information S1), deform the Surfaces 2–4 (Figures 5b–5d). Crossing Quaternary channels exhibit right-lateral deflections averaging 68 m along N15°W scarps and left-lateral deflection averaging 77 m along N15°E scarps. A monocline is observed at the southern tip of this section near Quebrada Soga, above a segment with suspected dominant reverse kinematics. Additionally, sparse N15°E fault scarps are visible further south. The described fault pattern is indicative of an array of dextral Riedel shears deforming younger aggradational surfaces. The decreasing surface expression of secondary faults and younger deformed surfaces suggests that the Camiña Fault has a southward propagation of reactivation, being more incipient between Quebrada Pinonave and Quebrada Aroma.

The Pampa de Camarones anticline is a key example of newly interpreted east-vergent structures within the Central Depression (Figure 6). This anticline consists of an array of N20-50° east-vergent monoclines, accompanied by secondary NNE-SSW extensional en echelon faults (Figures 6a and 6b). The Pampa de Camarones Anticline has caused the uplift and westward tilting of the Surfaces 4–5. The extensional secondary faults on top of these monoclines have created small, sharp graben structures. The presence of synthetic minor folds with similar oblique secondary features in the footwall of this anticline and its continuation southward suggests a distributed reactivation of similar structures across the Pampa de Camarones, Chiza, and Suca interfluves (Figure 6a). Quaternary channels crossing these structures have an average of 90 m of right-lateral deflection along N-S striking and 87 m of left-lateral deflection along NE-SW striking segments. The overall deformation pattern of the monoclines and observed sense of deflection of alluvial streams along secondary faults suggest that the last reactivation of the faults beneath the Pampa de Camarones and similar structures involved a dextral component.

Similar monoclines associated with reverse blind faults uplifting patches of Surface 5 are found in southern interfluves (Figures 4a and 7). Notable examples include the NW-SE striking Pampa de Tana Anticline and NNW-SSE striking Pampa de Tiliviche Fault. The Pampa de Tana Anticline is characterized by a steeper east-facing limb and a more subtle west-facing limb. Structural data indicate that the west-facing frontal monocline transitions into distributed dextral faults linked to the northern tip of the Pampa de Tiliviche Fault (Figures 4a and 5a and 5b). Outcrop observations reveal the complex fault geometry and expose positive flower structures deforming Upper Miocene rocks of the El Diablo Formation in both the Pampa de Tana Anticline (Figures 6c and 6d) and the Pampa de Tiliviche Fault (Figures S8c and S8d in Supporting Information S1). Lower vertical offsets

Figure 4. Fault inventory of the study area highlighting relevant newly mapped structures. (a) Newly observed and interpreted major structures. Stereonets show newly collected structural data. (b) Length-weighted frequency of fault and fracture orientation in each of the morphostructural units. (c) Distribution of fault and fracture lengths in each of the morphostructural units. AF = Aroma Fault; ArF = Aroma Flexure; AlFS = Alejo Fault System; AtaF = Atajaña Fault; CaF = Camarones Fault; CF= Camiña Fault; CcF = Calacala Flexure; GF = Garza Flexure; HF = Humayani Flexure; MF = Moquella Flexure; NFS = Negrito Fault System; PCA = Pampa de Camarones Anticline; PF = Pisagua Fault; PTA = Pampa de Tana Anticline; PTF = Pampa de Tiliviche Fault; QF = Quistagama Fault; OA = Oxaya Antilcine; SF = Soga Flexure; SM = Sucuna Monocline; SoF = Soga Fault; TaF = Tamarugal Fault. Map scale is 1; 500,000.

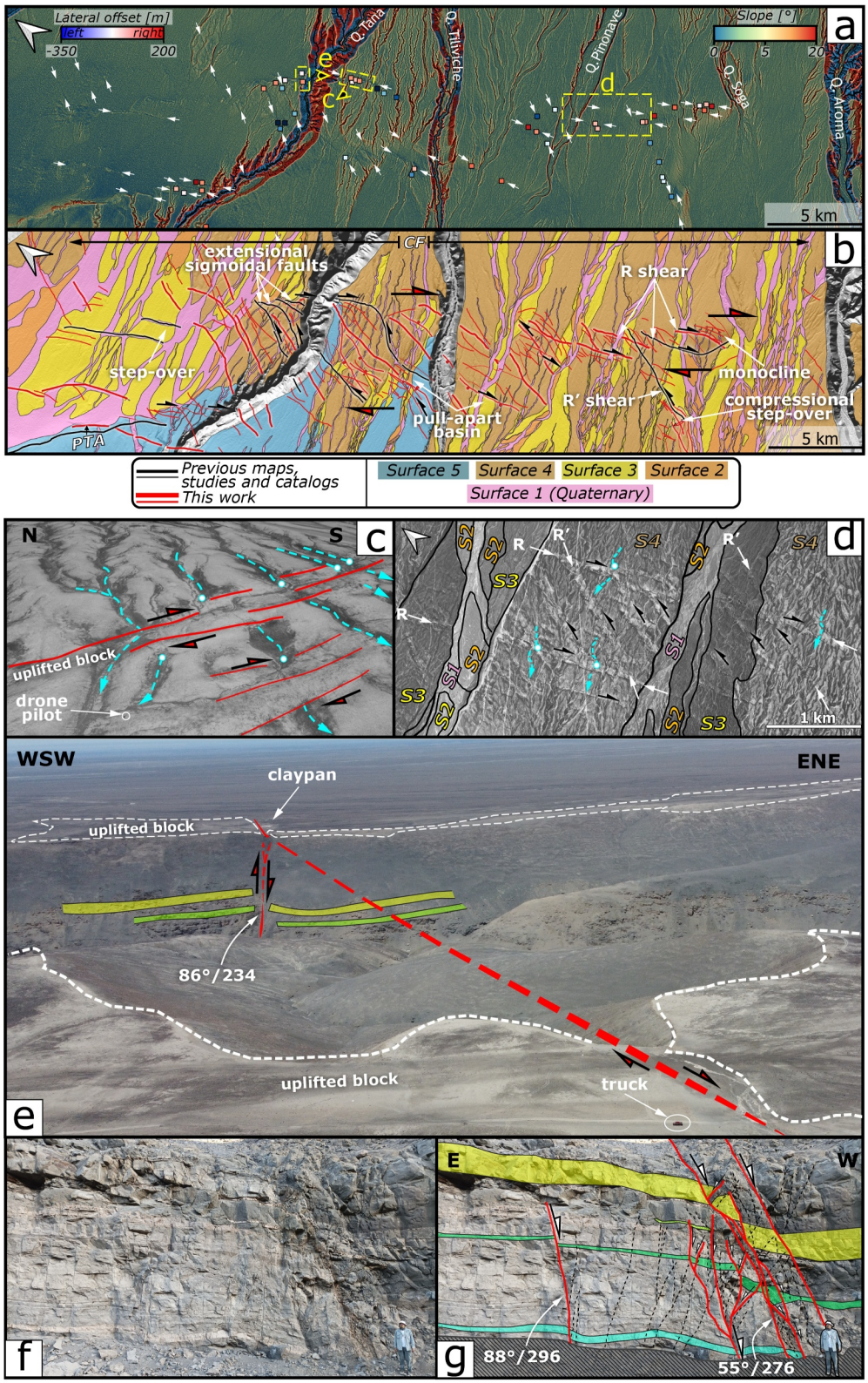
Lateral offset [m]
left
right
-350
200
Q. Tana
Q. Tilviche
Q. Pinonave
Slope [°]
0
5
20
Q. Soga
Q. Aroma
a
e
c
d
5 km
b
CF
extensional sigmoidal faults
R shear
step-over
monocline
R' shear
compressional step-over
pull-apart basin
PTA
5 km
Previous maps, studies and catalogs
This work
Surface 5
Surface 4
Surface 3
Surface 2
Surface 1 (Quaternary)
N
S
c
uplifted block
drone pilot
R
R'
S1
S2
S3
S4
d
1 km
WSW
ENE
claypan
uplifted block
86°/234
uplifted block
truck
e
E
W
f
g
88°/296
55°/276

Figure 5.

along the fault tips have allowed Quaternary streams to incise into the southern Pampa de Tana Anticline and northern Pampa de Tiliviche Fault hanging walls (Figure 7). Further south, smaller east-vergent monoclines, such as the Tamarugal and Soga Faults (Figures 4a and S8e and S8f in Supporting Information S1), deform Surfaces 4-3. The Soga Fault is linked to a NE-SW antithetic Riedel shear branching from the Camiña Fault (Figure 7).

In areas where trunk rivers expose Mesozoic rocks, the deeper sections of the flexures and underlying faults are observed (Figures 6e and 6f). For example, the faults beneath the Moquella Flexure and the Quisagama Fault zone are characterized by cataclastic fault cores of tens of centimeters wide and a damage zone with pervasive alteration of Mesozoic volcanoclastic rocks (Figure S9 in Supporting Information S1). A similar fault core was observed beneath the Pisagua Fault scarp (Figure 6f).

4.2. Quantification of Vertical and Strike-Slip Displacement Rates of East-Vergent Structures

The east-vergent structures deforming the Central Depression present variable net surface offsets, but a trend of southward decreasing values is observed along the study area, with each fault presenting higher offsets in its central segment (Figures 7a and 7b).

From north to south, the mean and maximum net vertical displacement rates along the Pampa de Camarones Anticline using the youngest available age marker (El Diablo Formation top surface age) are 6.1 ± 2 m/Ma and 11.5 ± 1.5 m/Ma, respectively. No Quaternary alluvial channels are found cutting through this structure hanging wall. Instead, a Quaternary depocenter is formed in its footwall, and streams deviate toward the north (Figure 6b). Along the monoclines in Pampa de Chiza, mean and maximum vertical displacement rates are 8.4 ± 1.4 m/Ma and 10.8 ± 1 m/Ma. No Quateranry alluvial channels are found on top of these structures, and they are being deviated southwards along the footwall instead.

The mean and maximum rates along the Pampa de Tana Anticline using the youngest available age marker (mean cosmogenic exposure age of 3.27 Ma) are 5.9 ± 1.5 m/Ma and 11.2 ± 0.8 m/Ma. A Quaternary depocenter has formed in the footwall of this anticline, and beheaded channels are observed crossing the structure where the net vertical displacement rates exceed 7.9 ± 0.8 m/Ma. The mean and maximum rates along the Pampa Tiliviche Fault using the youngest available age marker (cosmogenic exposure age of 3.19 Ma) are 4.5 ± 0.7 m/Ma and 6.9 ± 0.1 m/Ma, respectively. A Quaternary basin has formed in the footwall of this fault, and beheaded channels are found where the net surface offset exceeds 4.9 ± 0.3 m/Ma to the south. Secondary strike-slip faults in its northern portion deflect Quaternary channels crossing the hanging wall.

The Tamarugal and Soga Faults exhibit the lowest vertical surface offsets. Using the youngest available age markers (El Diablo Formation top surface age and an exposure age of 7.05 Ma, respectively), the mean and maximum vertical displacement rates for these faults are 1.5 m ± 0.1 m/Ma and 2.65 ± 0.1 m/Ma. Quaternary channels eroded these subtle folds and fault scarps, leaving patches of uplifted Surfaces 5-4.

The deflection of Quaternary alluvial channels is predominantly associated with distributed secondary synthetic, en echelon dextral faults along the east-vergent structures (Figure 7). The mean Quaternary right-lateral displacement rate in the study area is 26.7 ± 3.5 m/Ma, with a maximum of 74.15 ± 16 m/Ma found along the Pampa de Camarones Anticline. Newly detected NW-SE dextral strike-slip faults in the Pampa Tiliviche Fault hanging wall have a mean displacement rate of 34.2 ± 4.5 m/Ma. The Tamarugal Fault deflects Quaternary alluvial channels in its northern segment, but no deflected streams were detected to the south or along the Soga Fault. Intensive channel deflection is observed where the net surface uplift of each fault is the lowest and near deeply incised trunk rivers. This is particularly evident between the Pampa de Tana Anticline and Pampa de Tiliviche Faults, suggesting a correlation between lower tectonic uplift and increased strike-slip activity that facilitates river incision (Figure 7c).

Figure 5. Geomorphic evidence of oblique reactivation of west-vergent structures. (a) Red Relief Map showing the imprint of subtle faulting on the alluvial surfaces. Location of field localities and zoom-in maps are framed by boxes (b) Interpretation of (a) showing the dense array of Riedel shears slightly offsetting drainages and highlighting the active Camiña Fault below the sedimentary cover. (c) Drone photography showing deflected and interrupted streams due to subtle fault activity (location marked in panel b). (d) Zoom in on (b) showing the ability to detect subtle tectonic activity from high-resolution DEMs (e) Outcrop of a blind and steeply west-dipping subsidiary fault of the Camina Fault offsetting the El Diablo Formation and producing a gentle monocline (f, g) Raw and interpreted outcrop image of oblique transtensional faults along the Calacala Flexure (location in Figure 4a).

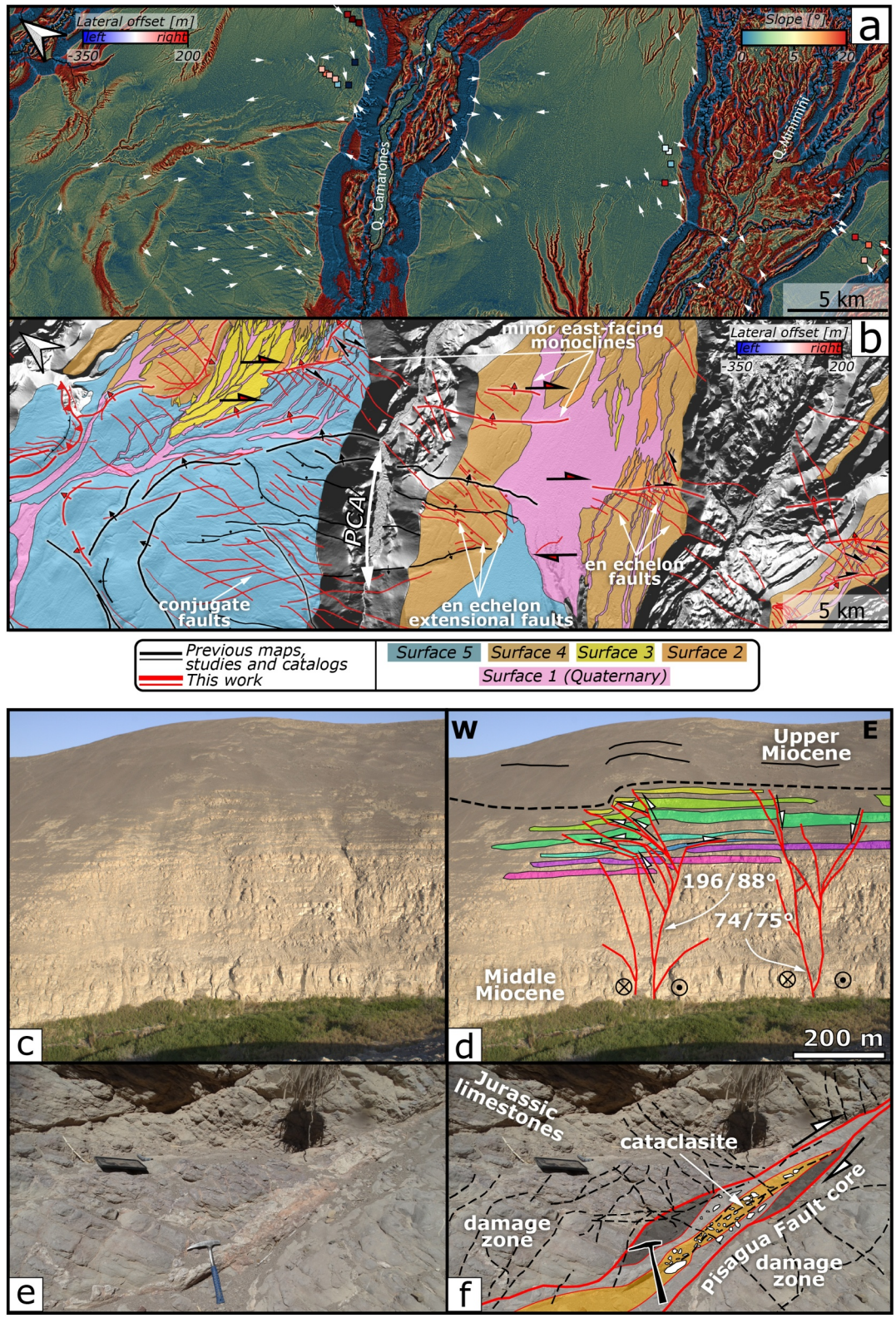

Figure 6. Geomorphic evidence of oblique reactivation of blind structures. (a) Red Relief Map with tectonic lineaments between white arrows. (b) Interpreted folds and secondary en echelon extensional faults and paleosurfaces. (c, d) Raw and interpreted outcrop images of compressive flower structure beneath the west-facing scarp of the Pampa de Tana Anticline and (e, f) Deep section of the Pisagua Fault (location in Figure 4a).

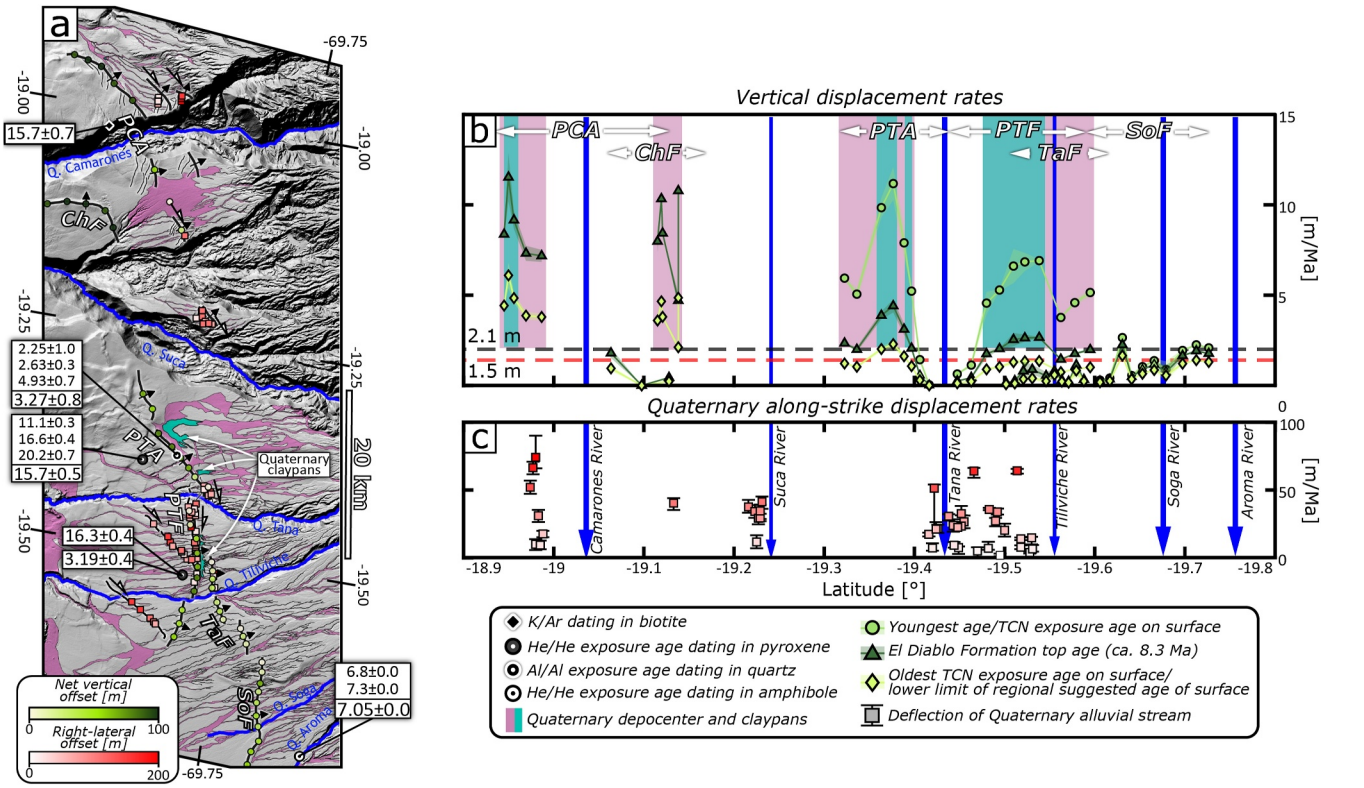

Figure 7. Calculation of vertical and along-strike displacement rates along east-vergent structures of the Central Depression. (a) Surface offset, river deflection, and location of age data used for rate calculations. (b) Calculated vertical displacement rates (c) Calculated along-strike displacement rates and location of trunk rivers. Dashed black and red lines in panel (b) represent Quaternary erosion, and deposition rates, respectively. ChF = Chiza Faults, PCA = Pampa de Camarones Anticline, PTA = Pampa de Tana Anticline, PTF = Pampa de Tiliviche Fault, SoF = Soga Fault, TaF = Tamarugal Fault.

4.3. Tectonically Driven Uplift Derived From Morphometric Drainage Analysis

The regional distribution of k_{snP} and knickpoints shows that trunk rivers and their tributaries reaching the Western Cordillera exhibit low k_{snP} values upstream of a main knickzone at the Precordillera. This knickzone is marked by 20 sharp tectonic knickpoints with an average elevation of 3,198 ± 341 m (Table S5 in Supporting Information S1), along with smaller non-tectonic knickpoints related to Miocene volcanic edifices (Figure 8). k_{snP} values increase rapidly downstream, peaking before reaching the Central Depression (Figure 8a). River concavity follows similar patterns with low concavity segments upstream of the Precordillera and high concavity across it (Figure 9a). These segments are separated by a slope-break zone shown in χ-elevation plots (Figure 9b). Tributaries confined to the Precordillera exhibit low k_{snP} values with slight increases related to west-vergent folds. A second slope-break zone is observed in the Tana River Basin, related to its coastal knickzone, which separates a low concavity-low k_{snP} segment in the Central Depression from a high-concavity-high k_{snP} coastal segment (Figure 9a). k_{snP} values by lithology suggest a minimal effect of lithologic contrast in drainage development across the study area, except for low values for Miocene volcanoes and high values for coastal granitoids and basalts (Figures 8b and S5 in Supporting Information S1). χ-elevation plots show that knickpoints related to the Miocene volcanoes have distributed χ values and do not mark slope-break zones (Figure 9).

The projection of the precordilleran paleo-profiles of all analyzed rivers results in a mean gained relief of 1,062 ± 331 m between these and the current outlets. The mean gained relief between the projection of the coastal segment of the Tana and Tiliviche Rivers the current outlet is 461 ± 24 m (Figure 9c). Minor tectonic knickpoints were found above the west-vergent Humayani and Garza Flexures and above the Camiña Fault. Other minor tectonic knickpoints are associated with the reverse Atajaña and Pisagua Faults (Figures 8a and 9). The Humayani and Garza Flexures and Camiña Fault produced a mean relief of 284 ± 98 m, 491 ± 7 m, and 12 ± 7 m, respectively. The mean relief of the Atajaña and Pisagua Faults are 80 ± 19 m and 71 ± 7, respectively (Figure 9c). No knickpoints related to the east-vergent structures across the Central Depression were detected.

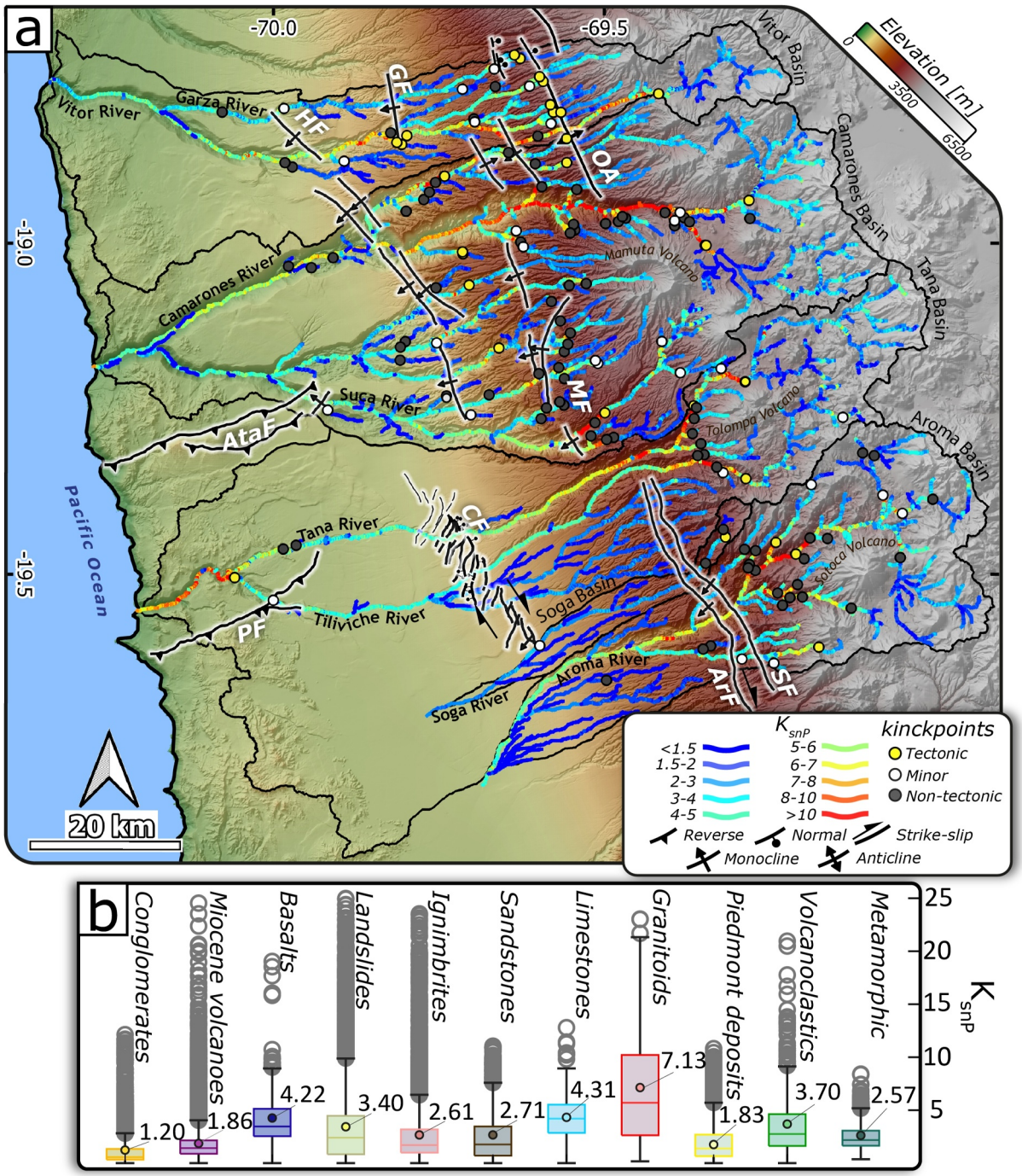

Figure 8. k_{snP} map and knickpoint distribution of major rivers in the study area. (a) k_{snP} and knickpoint distribution of the study area. Structures related to tectonic and minor knickpoints are shown. (b) k_{snP} values and mean values grouped by lithology. ArF = Aroma Flexure; AtaF = Atajaña Fault; CF = Camiña Fault; GF = Garza Flexure; HF = Humayani Flexure; MF = Moquella Flexure; OA = Oxaya Anticline; PF = Pisagua Fault.

5. Discussion

5.1. Detection of Reactivated Faults in Sediment-Covered Landscapes

Secondary structures on top of the Camiña Fault monocline were previously identified as scattered short structures with unknown kinematics (Pinto et al., 2004; Santibáñez et al., 2019). Our results unveiled a multitude of additional arrays of en-echelon faults and fractures along the monoclines of the Central Depression (Figures 5

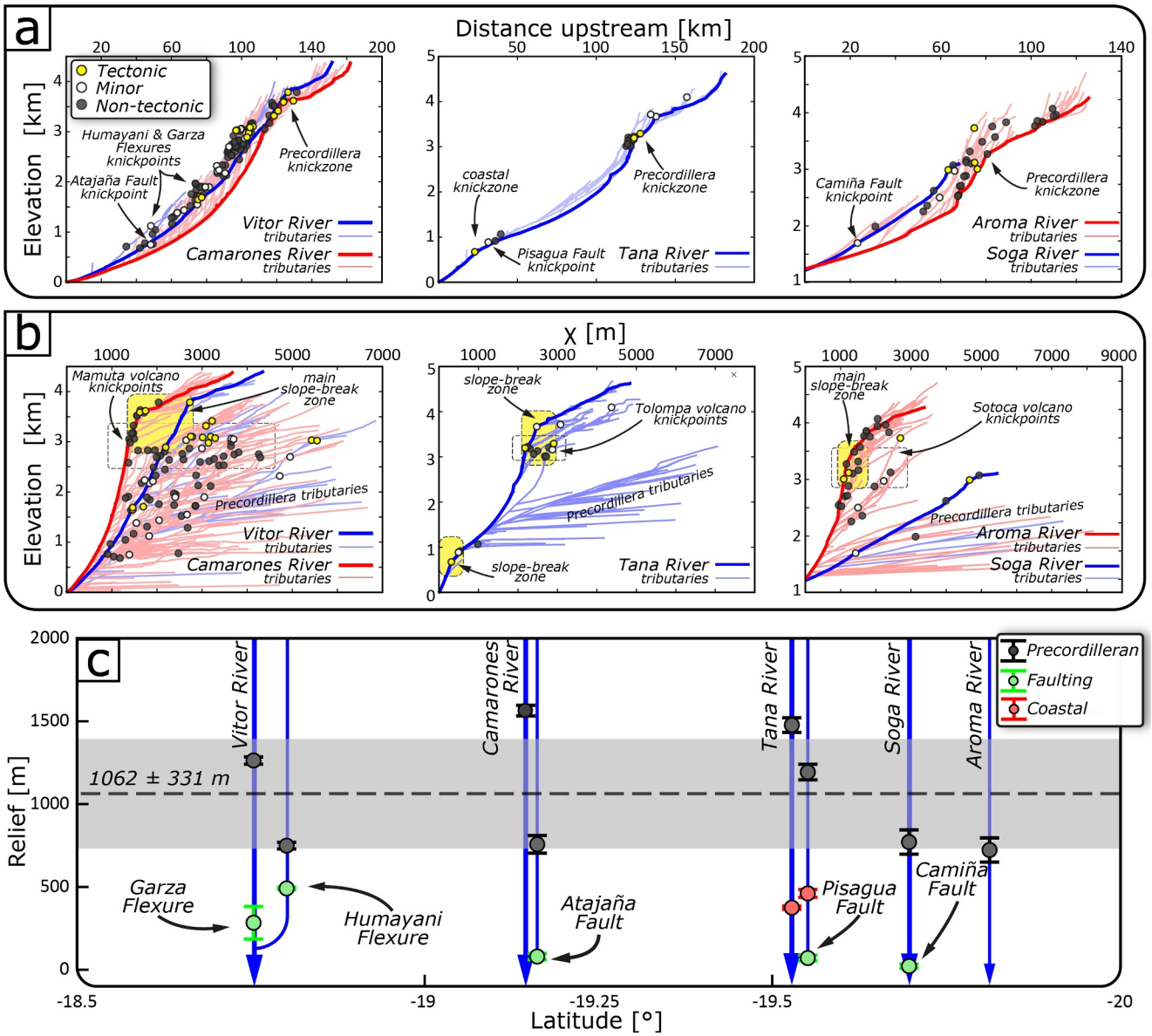

Figure 9. Morphometric analysis and paleo-profile projection of trunk rivers and tributaries. (a) Longitudinal profiles of major river drainage networks of the study area. (b) chi-elevation plots corresponding to the longitudinal profiles above. Drainage networks are separated for visual clarity and to highlight their different disequilibrium profiles. (c) Relief between current outlets and the outlet elevation of the Precordilleran paleo-profile projection of major river trunks and main tributaries. The dashed lines and shaded area mark the average relief between the Precordillera and the Central Depression.

and 6). This finding suggests that the underlying blind faults across the study area can be mapped through careful detection and interpretation of secondary fault scarps and fracture patterns. The fluvial incision across the Central Depression is too low to expose deep levels of faults beneath these monoclines. Yet, the observed fault zones in Mesozoic rocks of precordilleran west-vergent monoclines and coastal faults display characteristics of mature faults (Figures 6e and 6f and S8g and S8h in Supporting Information S1) (Ben-Zion & Sammis, 2003; Chester & Logan, 1986; Yang, 2015). Several studies suggest that faults across the forearc are inherited from Mesozoic times and inverted in several compressive events since the Upper Cretaceous (e.g., Allmendinger et al., 2005; Farías et al., 2005; García & Fuentes, 2012). Inverted Mesozoic normal faults beneath Central Depression are observed in seismic sections between ca. 21–25°S latitude (Fuentes et al., 2023; Martínez et al., 2021). Shallow seismicity with strike-slip focal mechanisms shows the oblique Quaternary reactivation of some of the same faults (González et al., 2021; Salazar et al., 2017). Therefore, it is likely that the newly detected subtle monoclines,

Riedel shear sand en-echelon arrays in the study area are linked to similar well-localized and reactivated faults originating during the Jurassic and Early Cretaceous.

The southward and more incipient reactivation of the Camiña Fault agrees with other exemplary field studies of blind transpressive basement faults, in which R shears and more pervasive en-echelon structures indicate incipient and well-developed segments of the same master fault, respectively (Ahlgren, 2001; Davis et al., 2000; Tindall & Davis, 1999). Analog experiments of oblique reactivation of single faults beneath a sedimentary cover show a similar structural evolution to that observed along the Camiña Fault (e.g., Casas et al., 2001; Deng et al., 2021; Dooley & Schreurs, 2012; Schreurs & Colletta, 1998). Our results emphasize the relevance of high-resolution fracture and secondary fault mapping as an important method to be included in the detection of potentially reactivated deep-seated faults concealed by alluvial sediments. This approach could be applied in similar desertic areas with subtle scarps and folds related to reactivated faults deforming arid alluvial plains, for example, the Western Argentine Precordillera (Peri et al., 2022) and Alborz Mountains in the northern Iranian Plateau (e.g., Kaveh-Firouz et al., 2023; Nazari et al., 2014).

5.2. Hidden Active Structures: Quantifying Displacement Rates in Relation to Erosion-Deposition Rates

Calculating vertical displacement rates in the study area proved challenging. Where possible, we used the youngest exposure age of the offset surfaces as an approximation for the minimum vertical displacement rate (Table S3 in Supporting Information S1). These results agree with previous Quaternary surface uplift estimations of ca. 12 m/Ma for the Pampa de Tana Anticline (Binnie et al., 2020) (Figure 7). No growth strata within the upper member of the El Diablo Formation were observed related to the activity of these faults, suggesting that the reactivation of east-vergent faults in the study area likely postdates the cessation of the deposition of the El Diablo Formation. By comparing fault structures with different quantified vertical displacement rates (Pampa de Tana Anticline: >10 m/Ma, Pampa de Tiliviche Fault: 5–10 m/Ma, and Tamarugal-Soga Faults: <5 m/Ma), we noticed key differences in drainage pattern development (Figure 10), from which we suggest three distinctive scenarios to qualitatively evaluate the rate of fault activity (Figures 10b and 10c):

1. In the first scenario, vertical displacement rates exceed Quaternary erosion and deposition rates, correlating with Quaternary depocenters and claypans (Figure 10b). Uplift rates outpace fluvial incision rates and Quaternary channels are easily beheaded. The uplifted paleo-channels are preserved in the hanging wall as windgaps and faults present well-developed scarps. The still active incoming channels pond along the footwall (Figure 10b). This scenario explains the intermediate sediment deposits on the interfluves of alluvial drainages sourcing from the Precordillera to the Central Depression in the study area (Figures 7 and 10).
2. In the second scenario, incision rates outpace deposition rates and are almost equal to the displacement rates, causing the streams to incise parallel to the fault scarp and leading to a strongly deviated flow (Figure 10c). The discharge from several incoming alluvial channels focuses on a single stream, which becomes strong enough to cut across the fault scarp, typically along the fault tips where displacement rates are low. If incision slightly exceeds displacement and deposition rates, runoff can keep pace with fault growth. Despite that incision occurs in unconsolidated alluvial deposits, the widespread gypsum crust of the Atacama Desert can bring enough bank stability to form narrow sinuous channels in tectonically uplifted regions before turning into wide braided channels downstream (Ritter et al., 2022), as observed in the study area (Figure 10c).
3. In the third scenario, reactivated faults with lower displacement rates than deposition rates correlate with warped and uplifted patches of older alluvial paleosurfaces, often accompanied by an array of en-echelon fractures reflecting the trace of the blind fault beneath (Figure 10d). Bufe et al. (2016) describe a similar scenario in low-sloping regions of the Tian Shan Range piedmont, resulting from the interplay between the high sediment flux of the alluvial channels and low uplift rates of the growing structure. The alluvial streams are capable of first cutting through the slow uplifting region (Humphrey & Konrad, 2000), then laterally widening their channels and leaving small patches of warped abandoned alluvial surfaces (Bufe et al., 2016, 2019).

These three scenarios are a good proxy for the detection of Quaternary blind or buried faults and their displacement rates and are consistent with pioneer studies on Quaternary active tectonics of blind compressive structures (e.g., Bullard & Lettis, 1993; Lettis et al., 1997). Identifying such structures is crucial for hazard assessment and our approach is applicable to regions where fault detection is hindered by thick sedimentary cover (Nicol et al., 2018), such as the Tien Shan Range foreland, the alluvial plains of the Greater Caucasus

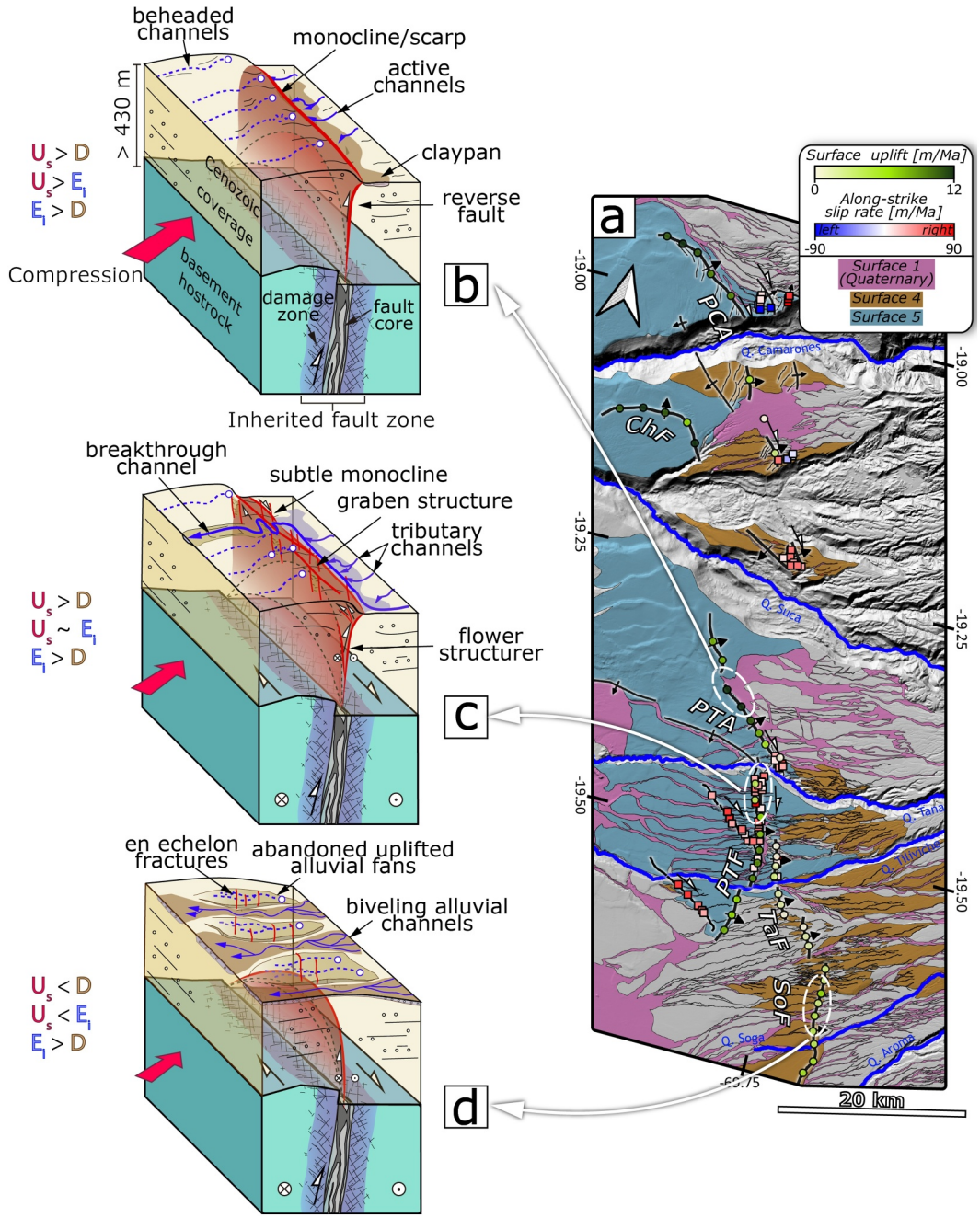

Figure 10. Block diagrams show the interaction between vertical displacement rate, deposition rate, and erosion rate and the effects of these on the development of drainage patterns. The thickness of the sedimentary cover corresponds to the Cenozoic thickness estimated in the TANA-1A well log. (a) Map view with locations of characteristic scenarios. (b) Scenario 1: Drainage development if deposition and incision rates are slower than vertical displacement rates. (c) Scenario 2: Drainage development if vertical displacement rates are higher than deposition rates and lower or close to incision rates. (c) Scenario 3: Drainage development if vertical displacement rates are lower than deposition and incision rates. D = Deposition rate; U_s = vertical displacement rate; E_i = Incision rate.

(Forte et al., 2015; Kaveh-Firouz et al., 2024) and slow-deforming regions of the Mongolian foreland (van der Wal et al., 2021). While further paleoseismological studies and additional age determinations are needed, identifying the deep-seated and active faults within our study area represents a significant contribution to the hazard assessment for the Northern Chile forearc.

5.3. New Insights From Major River Morphometrics Analysis

The resulting k_{snP}, concavity analysis, and major knickpoint locations (Figures 7 and 8) agree with previous studies suggesting that trunk rivers profiles reflect a transient response to a rapidly gained relief along the Precordillera relative to the Central Depression (Hoke et al., 2007; Norton & Schlunegger, 2011; Schildgen et al., 2007, 2009). The distribution of lithologic knickpoints and variations in k_{snP} by lithology (Figure 8b) support a sealing effect along the Precordillera due to the formation of large Middle Miocene to Upper Miocene volcanoes, reducing incision power of trunk rivers and leading to low-concavity and low-sloping upstream segments (Abbühl et al., 2011). Increased k_{snP} values related to granitoids and basalts are clustered along the coastal knickzone of the Tana River (Figure S5 in Supporting Information S1). The Tana River catchment area is almost twice the Vitor River Basin (Table 1), and the lithology at their outlets is similar. Thus, the increased k_{snP} values and the presence of the coastal knickzone are, in fact, more likely attributed to an uplift-precipitation interplay than a lithological effect.

Our estimated gained relief of 1,062 ± 331 m between the Precordillera and Central Depression falls within the range of the tectonic uplift suggested by Hoke et al. (2007) (Figure 9c). Slight differences in paleo-stream projections can be attributed to the selected reaches used for the projections (e.g., Clementucci, Ballato, Siame, Fox, et al., 2023) and differences in the accuracy and resolution of the digital topographic data sets employed.

These observations encourage us to interpret the newly detected minor tectonic knickpoints and gained relief above the west-vergent Humayani and Garza Flexures, Camiña Fault, and the east-west striking Atajaña and Pisagua Faults as a consequence of young fault-related tectonic uplift (Figures 8 and 9). These knickpoints have migrated only ca. 2.5 km upstream from the flexures hinge and faults scarps. This Late Cenozoic slow migration of the knickpoints has been attributed to the current predominant hyperarid conditions (Garcia et al., 2011). Thus, it is likely that the activity of these faults postdates the regional uplift of the High Andes relative to the Central Depression, which ceased around 7 Ma (Norton & Schlunegger, 2011). The minimum suggested age for river incision in the Camarones Basin at the Central Depression is 6.4 Ma (Hoke et al., 2007). Consequently, the vertical displacement rates of the Humayani and Garza Flexures, and Atajaña Fault since river incision and knickpoint formation are 79.7 ± 1 m/Ma, 44.4 ± 15.3 m/Ma, and 12.5 ± 1.1 m/Ma, respectively. The same rates calculated for the Pisagua and Camiña Faults yield 23.7 ± 2.3 m/Ma and 4.1 ± 0.4 m/Ma since river incision and draining of the Tiliviche paleolake at ca. 3 Ma (Kirk-Lawlor et al., 2013). These displacement rates are significantly higher than those for the east-vergent structures, suggesting that the activity of the latter ones has been largely obliterated by trunk river incision, except for the Soga River, which has a much lower incision power.

5.4. Late Cenozoic to Recent Tectonic Evolution of the Central Depression

The tectonic evolution of the Central Depression, as observed in this study, is complex, but can be divided into two regions based on the vergence of the structures (Figure 11a). In the eastern Central Depression, the Late Cenozoic evolution is dominated by the reactivation of west-vergent reverse faults, which began after ca. 7 Ma (Figure 11b) (García et al., 2002, 2011, 2013). This reactivation was likely triggered by increased convergence obliquity along the Arica Bend (Allmendinger & González, 2010; Farías et al., 2005; Somoza, 1998). The dextral transpressive kinematics of the Camiña Fault fit well into this stress regime. Furthermore, the more recent activity at <4.3 Ma of this fault, compared to the other west-vergent structures along the Precordillera, is consistent with the westward younging reactivation of the West Vergent Thrust System (Farías et al., 2005; Victor et al., 2004). Small right-lateral displacement of alluvial channels (Figure 5) attests that the Camiña Fault is slow but still active during the Quaternary.

In the western Central Depression, the reactivation of east-vergent structures can be summarized in two stages: (a) The northern half of the study area likely experienced the first reactivation of east-vergent faults, alongside NE-SW sinistral to transtensional coastal faults, uplifting the piedmont across the Pampa de Camarones and Pampa de Suca interfluves. This occurred probably after ca. 8.3 Ma and before the deep incision in the Camarones Basin (Figure 7a). (b) The reactivation continued as transpressively southward across the Pampa de Tana and Pampa del Tamarugal interfluves, accompanied by ENE-WSW reverse faults. This stage most likely occurred before 5.6 Ma (Binnie et al., 2020), prior to the draining of the Tiliviche Paleolake (Kirk-Lawlor et al., 2013), and persisted until at least after ca. 2 Ma, which is the age of the youngest dated abandoned channel on top of the Pampa de Tana Anticline (Binnie et al., 2020). These east-vergent faults caused the inversion of the Andean piedmont, forming a topographic barrier to the drainage networks prior to their deep incision across the Central Depression. Low

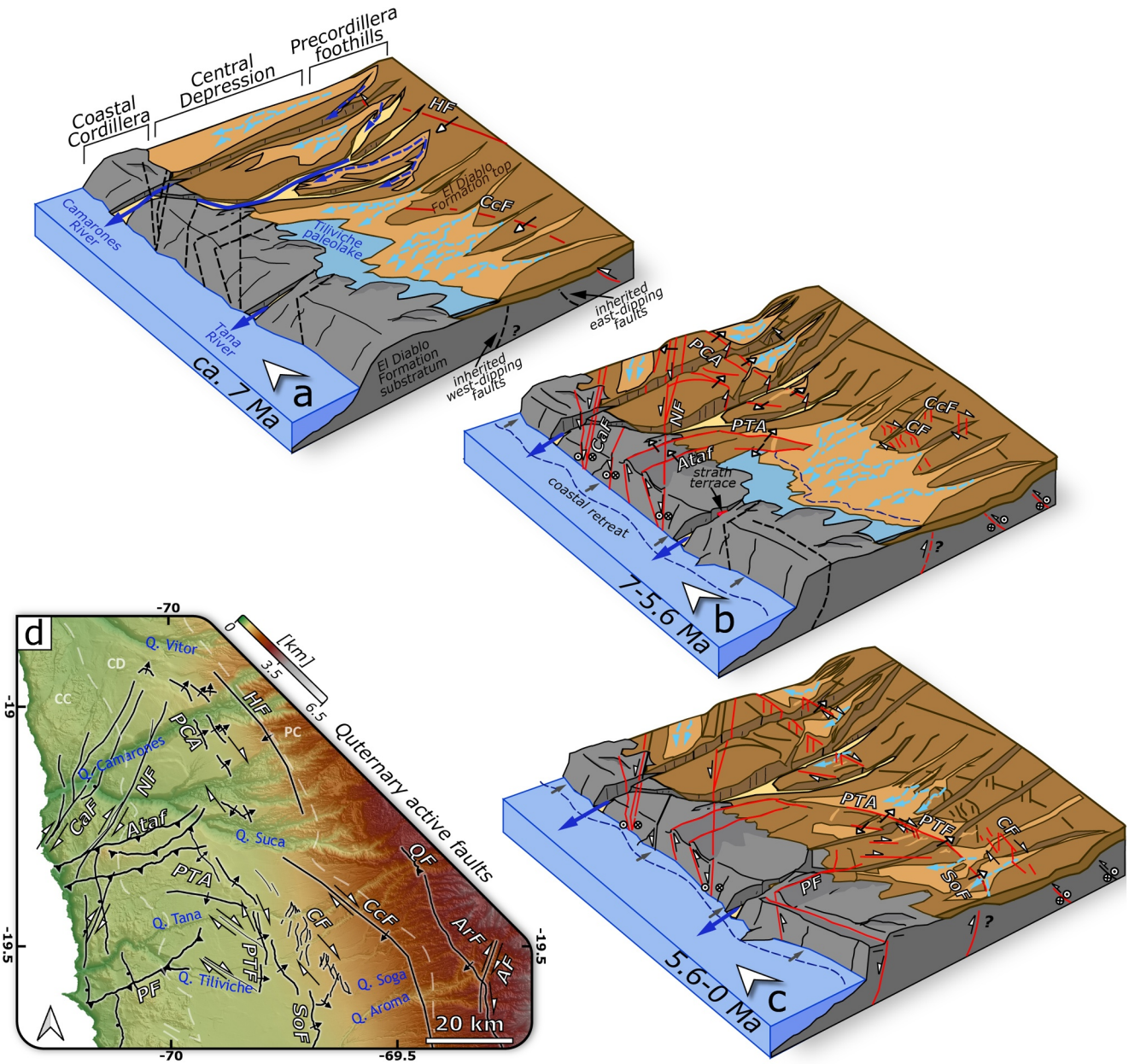

Figure 11. Block diagrams depicting the Late Cenozoic landscape evolution in the Central Depression in the study area. (a) Minor folding above faults of Western Vergent Thrust System started after ca. 7 Ma and the incision of the Camarones River started at a minimum age of ca. 6.4 Ma. The Tana River has been blocked at the eastern boundary of the Coastal Cordillera since ca. 10 Ma, producing the Tiliviche Paleolake. (b) East-vergent structures, NE-SW, and ENE-WSW faults are reactivated in the northern part of the study area. Possible contemporaneous coastal uplift left a strath terrace at the Tana River. Incision of the Camarones River continues, and the Tiliviche Paleolake has reduced its extension, due to increased aridity and drainage modification. Reactivation of the transpressive Camiña Fault and other west-vergent reverse faults is intensified in the eastern Central Depression (c) The reactivation of east-vergent faults propagates to the south at 5.6–3 Ma, producing uplift of the western Central Depression. Camiña Fault reactivation also propagates southward. Deep incision of the Tana River drainages started at <3 Ma, and the Tiliviche Paleolake is completely drained by knickpoint migration, drainage modification, and aridification. (d) Map of most important Quaternary active faults for reference. AF = Aroma Fault; ArF = Aroma Flexure; AtaF = Atajaña Fault; CaF = Camarones Fault; CC = Coastal Cordillera; CcF = Calacala Flexure; CD = Central Depression; CF = Camiña Fault; HF = Humayani Flexure; NF = Negrito Fault; PC = Precordillera; PCA = Pampa de Camarones Anticline; PTA = Pampa de Tana Anticline; PTF = Pampa de Tiliviche Fault; SoF = Soga Fault.

incision rates in the Tana River and southern rivers allowed faults to redirect streams toward their tips, where vertical displacement rates are <1 m/Ma (Figure 11c). Displaced and beheaded Quaternary alluvial channels attest that the Pampa de Tiliviche Fault was active in Quaternary times, alongside the Pampa de Tana Antilcine (Figure 10b).

The timing and kinematics of the reactivation of the east-vergent structures, with a strong oblique component, are similar to the reactivation of the transpressive structures in the West Vergent Thrust System (Farias et al., 2005; Legrand et al., 2007). However, the Late Cenozoic westward advance of this fault system at this latitude conflicts with the stress regime of the Coastal Cordillera indicated by its complex fault patterns intruding to the Central Depression and the east-vergence of structures in the western Central Depression (Figures 2, 4 and 11). Deep seismicity shows N-S compressive stresses across the coastal forearc and into the western Central Depression, with dextral strike-slip moment tensor solutions in the southern half and sinistral strike-slip solutions in the northern half (Herrera et al., 2021) (Figure 2a). This is compatible with the ENE-WSW reverse faults, the reverse to transpressive dextral kinematic of NW-SE and NNW-SSE Quaternary faults, and the sinistral kinematics of NE-SW fault systems in the northwestern portion of the study area (Figures 11d and S9 in Supporting Information S1). Therefore, the southward propagating uplift of the western Central Depression (Figures 11a–11c) is most likely governed by the reactivation of the east-vergent faults which constrain the coastal block deformation. The tectonic evolution and current fault kinematics of the study area suggest an along-trench tectonic segmentation of the coastal forearc close to the Arica Bend, which is suggested to be expressed in contrasting fault patterns (Boutelier et al., 2014; Boutelier & Oncken, 2010).

6. Conclusions

1. We detected formerly unmapped active faults across the sediment-covered landscape of the Central Depression and Precordilleran foothills. These faults, primarily subsidiary faults and monoclines, exhibit numerous secondary en-echelon fracture arrays deforming Late Cenozoic to Quaternary surfaces. They are diagnostic of well-localized reactivated blind mature faults inherited from Mesozoic times.
2. Two different main fault systems are present in the Central Depression distinguishable by their vergence: the West Vergent Thrust System to the east, and an east-vergent fault system in the western Central Depression. Vertical displacement rates for the east-vergent fault system are in the order of <12 m/Ma in agreement with previous estimates for the Pampa de Tana Anticline and are potentially higher depending on the exact onset of displacement.
3. The timing and kinematics of reactivation of both the east-vergent and West Vergent Thrust Systems align with the Late Miocene-Pliocene onset of oblique subduction along the Arica Bend. The incremental activity of the east-vergent fault system is strongly linked to the ongoing tectonic evolution of the Coastal Cordillera. These faults inverted the Andean piedmont, modifying the drainage patterns of the study area until at least 2 Ma.
4. We quantified the interaction between vertical displacement, erosion, and deposition rates for six key faults by carefully analyzing the subtle drainage pattern changes. We propose three scenarios for evaluating Quaternary tectonic activity, especially in areas where structural observation is hampered by sedimentary covers. The newly detected faults identified during this study represent an under-recognized seismic hazard, warranting further investigation, including the dating of geomorphic markers and paleoseismological studies.

Data Availability Statement

The fault and fracture database, mapped paleosurfaces, as well as compilated cosmogenic exposure ages and dating ages for geologic markers, are available for download in Supporting Information S2 and from the GFZ Data Services repository (Vega-Ruiz et al., 2024).

Acknowledgments
This work was funded by the Deutsche Forschungsgemeinschaft (DFG, German Research Foundation)—Projekt number 268236062—CRC 1211. We are very grateful to Eduardo Campos and Damian Lopez for the crucial logistic support. We also thank Vanessa Steinritz for contributing to the database confection and Ricardo Aguilera, Sara Pena-Castellnou, and Gonzalo Moreno for their assistance in the field. Also, we thank the careful and constructive review by Gregory De Pascale, Robin Lacassin, and two anonymous reviewers who helped to improve this manuscript remarkably. Open Access funding enabled and organized by Projekt DEAL.

References

Abbühl, L. M., Norton, K. P., Jansen, J. D., Schlunegger, F., Aldahan, A., & Possnert, G. (2011). Erosion rates and mechanisms of knickzone retreat inferred from 10Be measured across strong climate gradients on the northern and central Andes Western Escarpment. *Earth Surface Processes and Landforms*, *36*(11), 1464–1473. https://doi.org/10.1002/ESP.2164

Adams, B. A., Whipple, K. X., Forte, A. M., Heimsath, A. M., & Hodges, K. V. (2020). Climate controls on erosion in tectonically active landscapes. *Science Advances*, *6*(42), 3166–3182. https://doi.org/10.1126/SCIADV.AAZ3166/SUPPL_FILE/AAZ3166_SM.PDF

Ahlgren, S. G. (2001). The nucleation and evolution of Riedel shear zones as deformation bands in porous sandstone. *Journal of Structural Geology*, *23*(8), 1203–1214. https://doi.org/10.1016/S0191-8141(00)00183-8

Allmendinger, R., González, G., Yu, J., Hoke, G., & Isacks, B. (2005). Trench-parallel shortening in the northern Chilean Forearc: Tectonic and climatic implications. *Geological Society of America Bulletin*, *117*(1), 89. https://doi.org/10.1130/B25505.1

Allmendinger, R. W., & González, G. (2010). Invited review paper: Neogene to Quaternary tectonics of the coastal Cordillera, northern Chile. *Tectonophysics*, *495*(1–2), 93–110. https://doi.org/10.1016/j.tecto.2009.04.019

Alpers, C. N., & Brimhall, G. H. (1988). Middle Miocene climatic change in the Atacama Desert, northern Chile: Evidence from supergene mineralization at La Escondida. *Geological Society of America Bulletin*, *100*(10), 1640–1656. https://doi.org/10.1130/0016-7606(1988)100<1640:MMCCIT>2.3.CO;2

Ammirati, J. B., Vargas, G., Rebolledo, S., Abrahami, R., Potin, B., Leyton, F., & Ruiz, S. (2019). The crustal seismicity of the western Andean thrust (Central Chile, 33°–34° S): Implications for regional tectonics and seismic hazard in the Santiago area. *Bulletin of the Seismological Society of America*, *109*(5), 1985–1999. https://doi.org/10.1785/0120190082

Amundson, R., Dietrich, W., Bellugi, D., Ewing, S., Nishiizumi, K., Chong, G., et al. (2012). Geomorphologic evidence for the late Pliocene onset of hyperaridity in the Atacama Desert. *Geological Society of America Bulletin*, *124*(7–8), 1048–1070. https://doi.org/10.1130/B30445.1

Armijo, R., Lacassin, R., Coudurier-Curveur, A., & Carrizo, D. (2015). Coupled tectonic evolution of Andean orogeny and global climate. *Earth-Science Reviews*, *143*, 1–35. https://doi.org/10.1016/j.earscirev.2015.01.005

Armijo, R., Rauld, R., Thiele, R., Vargas, G., Campos, J., Lacassin, R., & Kausel, E. (2010). The West Andean thrust, the San Ramón fault, and the seismic hazard for Santiago, Chile. *Tectonics*, *29*(2). https://doi.org/10.1029/2008tc002427

Arrowsmith, R. J., Crosby, C. J., Korzhenkov, A. M., Mamyrov, E., Povolotskaya, I., Guralnik, B., & Landgraf, A. (2017). Surface rupture of the 1911 kebin (Chon-Kemin) earthquake, Northern tien Shan, Kyrgyzstan. *Geological Society - Special Publications*, *432*(1), 233–253. https://doi.org/10.1144/SP432.10/ASSET/1D1C15E0-4B47-4B8A-840C-FD7F88BA95D2/ASSETS/GRAPHIC/SP432-1500F13.JPEG

Audin, L., David, C., Hall, S., Farber, S., & Hérail, G. (2006). Geomorphic evidences of recent tectonic activity in the forearc, southern Peru. *Revista de la Asociación Geológica Argentina*, *61*(4), 545–554. Retrieved from http://www.scielo.org.ar/img/revistas/raga/v61n4/html/v61n4a09.htm

Audin, L., Herail, G., Riquelme, R., Darrozes, J., Martinod, J., & Font, E. (2003). Geomorphological markers of faulting and neotectonic activity along the western Andean margin, northern Chile. *Journal of Quaternary Science*, *18*(8), 681–694. https://doi.org/10.1002/jqs.787

Benavente, C., Palomino, A., Wimpenny, S., García, B., Rosell, L., Aguirre, E., et al. (2022). Paleoseismic evidence of the 1715 C.E earthquake on the Purgatorio Fault in Southern Peru: Implications for seismic hazard in subduction zones. *Tectonophysics*, *834*, 229355. https://doi.org/10.1016/j.tecto.2022.229355

Benavente, C., Zerathe, S., Audin, L., Hall, S. R., Robert, X., Delgado, F., et al. (2017). Active transpressional tectonics in the Andean forearc of southern Peru quantified by ^{10}Be surface exposure dating of an active fault scarp. *Tectonics*, *36*(9), 1662–1678. https://doi.org/10.1002/2017TC004523

Ben-Zion, Y., & Sammis, C. G. (2003). Characterization of fault zones. *Pure and Applied Geophysics*, *160*(3–4), 677–715. https://doi.org/10.1007/PL00012554/METRICS

Binnie, S. A., Reicherter, K. R., Victor, P., González, G., Binnie, A., Niemann, K., et al. (2020). The origins and implications of paleochannels in hyperarid, tectonically active regions: The northern Atacama Desert, Chile. *Global and Planetary Change*, *185*, 103083. https://doi.org/10.1016/j.gloplacha.2019.103083

Blanco, N., & Tomilson, A. (2013). Carta Guatacondo, Región de Tarapacá. *Servicio Nacional de Geología y Minería, Carta Geológica de Chile, Serie Geología Básica*, *156*(1).

Boutelier, D., Oncken, O., & Cruden, A. R. (2014). Trench-parallel shortening in the forearc caused by subduction along a seaward-concave plate boundary: Insights from analogue modelling experiments. *Tectonophysics*, *611*, 192–203. https://doi.org/10.1016/J.TECTO.2013.11.028

Boutelier, D. A., & Oncken, O. (2010). Role of the plate margin curvature in the plateau buildup: Consequences for the central Andes. *Journal of Geophysical Research*, *115*(B4), 4402. https://doi.org/10.1029/2009JB006296

Bozkurt, D., Rondanelli, R., Garreaud, R., & Arriagada, A. (2016). Impact of warmer eastern tropical Pacific SST on the March 2015 Atacama floods. *Monthly Weather Review*, *144*(11), 4441–4460. https://doi.org/10.1175/MWR-D-16-0041.1

Buddin, T. S., Stimpson, I. G., & Williams, G. D. (1993). North Chilean forearc tectonics and cenozoic plate kinematics. *Tectonophysics*, *220*(1–4), 193–203. https://doi.org/10.1016/0040-1951(93)90231-8

Bufe, A., Paola, C., & Burbank, D. W. (2016). Fluvial bevelling of topography controlled by lateral channel mobility and uplift rate. *Nature Geoscience*, *9*(9), 706–710. https://doi.org/10.1038/ngeo2773

Bufe, A., Turowski, J. M., Burbank, D. W., Paola, C., Wickert, A. D., & Tofelde, S. (2019). Controls on the lateral channel-migration rate of braided channel systems in coarse non-cohesive sediment. *Earth Surface Processes and Landforms*, *44*(14), 2823–2836. https://doi.org/10.1002/ESP.4710

Bullard, T. F., & Lettis, W. R. (1993). Quaternary fold deformation associated with blind thrust faulting, Los Angeles Basin, California. *Journal of Geophysical Research: Solid Earth*, *98*(B5), 8349–8369. https://doi.org/10.1029/93JB00012

Carbonneau, P. E., & Dietrich, J. T. (2017). Cost-effective non-metric photogrammetry from consumer-grade sUAS: Implications for direct georeferencing of structure from motion photogrammetry. *Earth Surface Processes and Landforms*, *42*(3), 473–486. https://doi.org/10.1002/ESP.4012

Carrizo, D., González, G., & Dunai, T. (2008). Constricción neógena en la Cordillera de la Costa, norte de Chile: Neotectónica y datación de superficies con 21Ne cosmogónico. *Revista Geologica de Chile*, *35*(1), 1–38. https://doi.org/10.4067/S0716-02082008000100001

Casas, A. M., Gapais, D., Nalpas, T., Besnard, K., & Román-Berdiel, T. (2001). Analogue models of transpressive systems. *Journal of Structural Geology*, *23*(5), 733–743. https://doi.org/10.1016/S0191-8141(00)00153-X

Chester, F. M., & Logan, J. M. (1986). Implications for mechanical properties of brittle faults from observations of the Punchbowl fault zone, California. *Pure and Applied Geophysics PAGEOPH*, *124*(1–2), 79–106. https://doi.org/10.1007/BF00875720/METRICS

Chiba, T., Suzuki, Y., & Hiramatsu, T. (2007). Digital terrain representation methods and red relief image map, A new visualization approach. *Map, Journal of the Japan Cartographers Association*, *45*(1), 27–36. https://doi.org/10.11212/jjca1963.45.27

Clark, M., Maheo, G., Saleeby, J., & Farley, K. (2005). The non-equilibrium landscape of the southern Sierra Nevada, California. *Geological Society of America Today*, *15*(9), 4. https://doi.org/10.1130/1052-5173(2005)15[4:TNLOTS]2.0.CO;2

Clementucci, R., Ballato, P., Siame, L., Fox, M., Lanari, R., Sembroni, A., et al. (2023). Surface uplift and topographic rejuvenation of a tectonically inactive range: Insights from the anti-atlas and the Siroua Massif (Morocco). *Tectonics*, *42*(2), e2022TC007383. https://doi.org/10.1029/2022TC007383

Clementucci, R., Ballato, P., Siame, L. L., Faccenna, C., Racano, S., Torreti, G., et al. (2023). Transient response to changes in uplift rates in the northern Atlas-Meseta system (Morocco). *Geomorphology*, *436*, 108765. https://doi.org/10.1016/J.GEOMORPH.2023.108765

Clementucci, R., Lanari, R., Faccenna, C., Crosetto, S., Reitano, R., Zoppis, G., & Ballato, P. (2024). Morpho-tectonic evolution of the southern Apennines and Calabrian arc: Insights from Pollino range and surrounding extensional intermontane basins. *Tectonics*, *43*(5), e2023TC008002. https://doi.org/10.1029/2023TC008002

Comte, D., Dorbath, C., David, C., Haessler, H., Correa, E., Balmaceda, I., & Cruz, A. (2003). Distribución temporal y en profundidad de las réplicas del sismo superficial de Aroma, norte de Chile del 24 de julio de 2001. In *biblioteca.sernageomin.cl*. Retrieved from https://biblioteca.sernageomin.cl/opac/DataFiles/ComteD_et_al.pdf

Cortés, J., Farías, M., Comte, D., & Charrier, R. (2012). Estructuras y depósitos neógenos de la región de Cariquima (Altiplano chileno): Implicancias en el origen de la Cordillera Occidental a los 19°30'S. *Congreso Geológico Chileno*, 229–231. Retrieved from https://catalogobiblioteca.sernageomin.cl/Archivos/14127_pp_229_231.pdf

Coudurier-Curveur, A., Lacassin, R., & Armijo, R. (2015). Andean growth and monsoon winds drive landscape evolution at SW margin of South America. *Earth and Planetary Science Letters*, *414*, 87–99. https://doi.org/10.1016/j.epsl.2014.12.047

Crosta, G. B., Hermanns, R., Frattini, P., Valbuzzi, E., & Valagussa, A. (2014). Large slope instabilities in northern Chile: Inventory, characterization and possible triggers. In *Landslide science for a safer geoenvironment: Volume 3: Targeted landslides* (pp. 175–181). Springer International Publishing.

Davis, G. H., Bump, A. P., García, P. E., & Ahlgren, S. G. (2000). Conjugate Riedel deformation band shear zones. *Journal of Structural Geology*, *22*(2), 169–190. https://doi.org/10.1016/S0191-8141(99)00140-6

Deng, H., McClay, K., & Bilal, A. (2021). Multiphase activation of the boundary fault system of the eastern Dampier subbasin, Northwest Shelf of Australia. *AAPG Bulletin*, *105*(1), 157–188. https://doi.org/10.1306/03022019160

Densmore, A. L., Ellis, M. A., Li, Y., Zhou, R., Hancock, G. S., & Richardson, N. (2007). Active tectonics of the Beichuan and Pengguan faults at the eastern margin of the Tibetan Plateau. *Tectonics*, *26*(4). https://doi.org/10.1029/2006TC001987

De Pascale, G. P. (2021). Comment on "Crustal faults in the Chilean Andes: Geological constraints and seismic potential" by, Andean geology 46 (1): 32-65. *Andean Geology*, *48*(1), 175–183. https://doi.org/10.5027/ANDGEOV48N1-3310

Diederich, J. L., Wennrich, V., Bao, R., Büttner, C., Bolten, A., Brill, D., et al. (2020). A 68 ka precipitation record from the hyperarid core of the Atacama Desert in northern Chile. *Global and Planetary Change*, *184*, 103054. https://doi.org/10.1016/J.GLOPLACHA.2019.103054

Dooley, T. P., & Schreurs, G. (2012). Analogue modelling of intraplate strike-slip tectonics: A review and new experimental results. In *Tectonophysics* (Vol. 574–575, pp. 1–71). Elsevier. https://doi.org/10.1016/j.tecto.2012.05.030

Dunai, T. J., González López, G. A., & Juez-Larré, J. (2005). Oligocene–Miocene age of aridity in the Atacama Desert revealed by exposure dating of erosion-sensitive landforms. *Geology*, *33*(4), 321. https://doi.org/10.1130/G21184.1

Evenstar, L. A., Hartley, A. J., Stuart, F. M., Mather, A. E., Rice, C. M., & Chong, G. (2009). Multiphase development of the Atacama Planation Surface recorded by cosmogenic 3He exposure ages: Implications for uplift and Cenozoic climate change in western South America. *Geology*, *37*(1), 27–30. https://doi.org/10.1130/G25437A.1

Evenstar, L. A., Mather, A. E., & Hartley, A. J. (2020). Using spatial patterns of fluvial incision to constrain continental-scale uplift in the Andes. *Global and Planetary Change*, *186*, 103119. https://doi.org/10.1016/j.gloplacha.2020.103119

Evenstar, L. A., Mather, A. E., Hartley, A. J., Stuart, F. M., Sparks, R. S. J., & Cooper, F. J. (2017). Geomorphology on geologic timescales: Evolution of the late Cenozoic Pacific paleosurface in northern Chile and southern Peru. *Earth-Science Reviews*, *171*, 1–27. https://doi.org/10.1016/j.earscirev.2017.04.004

Farías, M., Charrier, R., Comte, D., Martinod, J., & Hérail, G. (2005). Late Cenozoic deformation and uplift of the western flank of the Altiplano: Evidence from the depositional, tectonic, and geomorphologic evolution and shallow seismic activity (northern Chile at 19°30′S). *Tectonics*, *24*(4). https://doi.org/10.1029/2004TC001667

Flint, J. J. (1974). Stream gradient as a function of order, magnitude, and discharge. *Water Resources Research*, *10*(5), 969–973. https://doi.org/10.1029/wr010i005p00969

Forte, A. M., & Whipple, K. X. (2019). Short communication: The topographic analysis Kit (TAK) for TopoToolbox. *Earth Surface Dynamics*, *7*(1), 87–95. https://doi.org/10.5194/ESURF-7-87-2019

Forte, A. M., Whipple, K. X., & Cowgill, E. (2015). Drainage network reveals patterns and history of active deformation in the eastern Greater Caucasus. *Geosphere*, *11*(5), 1343–1364. https://doi.org/10.1130/GES01121.1

Fuentes, G., Perroud, S., Garrido, W., Quiroga, R., & Martínez, F. (2023). Along strike variations on inverted Tarapacá Basin and its influence in buried western Andean mountain front building. *Journal of South American Earth Sciences*, *128*, 104417. https://doi.org/10.1016/j.jsames.2023.104417

Gallardo, A. (1962). Informe Geológico Pozo: TANA N°1-A.

Gallen, S., Wegmann, K., & Bohnenstiehl, D. (2013). Miocene rejuvenation of topographic relief in the southern Appalachians. *Geological Society of America Today*, *23*(2), 4–10. https://doi.org/10.1130/GSATG163A.1

Galli-Olivier, C. (1967). Pediplain in northern Chile and the Andean uplift. *Science*, *158*(3801), 653–655. https://doi.org/10.1126/science.158.3801.653

García, M., & Fuentes, G. (2012). Carta Cuya, regiones de Arica y Parinacota y de Tarapacá. Servicio Nacional de Geología y Minería, Carta Geológica de Chile, Serie Geología Básica, 146.

García, M., Fuentes, G., & Riquelme, F. (2013). Carta Miñimiñi, Regiones de Arica y Parinacota y de Tarapacá. Servicio Nacional de Geología y Minería, Carta Geológica de Chile, Serie Geología Básica, 157.

García, M., Gardeweg, M., Clavero, J., & Hérail, G. (2004). *Hoja Arica, Región de Tarapacá: Servicio Nacional de Geología y Minería, Carta Geológica de Chile, Serie Geología Básica*, *84*. *1 mapa escala 1: 250.000*.

García, M., Hérail, G., Charrier, R., Mascle, G., Fornari, M., & Perez de Arce, C. (2002). Oligocene-Neogene tectonic evolution of the Altiplano of northern Chile (18-19°s). In *5th international symposium of Andean geodynamics, (ISAG 2002, Toulouse)* (pp. 235–238).

García, M., Maksaev, V., Townley, B., & Dilles, J. (2017). Metallogeny, structural evolution, post-mineral cover distribution and exploration in concealed areas of the northern Chilean Andes. *Ore Geology Reviews*, *86*, 652–672. https://doi.org/10.1016/j.oregeorev.2017.01.025

García, M., Riquelme, R., Farías, M., Hérail, G., & Charrier, R. (2011). Late Miocene–Holocene canyon incision in the western Altiplano, northern Chile: Tectonic or climatic forcing? *Journal of the Geological Society*, *168*(4), 1047–1060. https://doi.org/10.1144/0016-76492010-134

Gelwick, K. D., Willett, S. D., & Yang, R. (2024). Geomorphic indicators of continental-scale landscape transience in the Hengduan Mountains, SE Tibet, China. *Earth Surface Dynamics*, *12*(3), 783–800. https://doi.org/10.5194/ESURF-12-783-2024

González, G., Cembrano, J., Carrizo, D., Macci, A., & Schneider, H. (2003). The link between forearc tectonics and Pliocene–Quaternary deformation of the Coastal Cordillera, northern Chile. *Journal of South American Earth Sciences*, *16*(5), 321–342. https://doi.org/10.1016/S0895-9811(03)00100-7

González, G., Gerbault, M., Martinod, J., Cembrano, J., Carrizo, D., Allmendinger, R., & Espina, J. (2008). Crack formation on top of propagating reverse faults of the Chuculay Fault System, northern Chile: Insights from field data and numerical modelling. *Journal of Structural Geology*, *30*(6), 791–808. https://doi.org/10.1016/J.JSG.2008.02.008

González, G., Pasten-Araya, F., Victor, P., González, Y., Valenzuela, J., & Shrivastava, M. (2021). The role of interplate locking on the seismic reactivation of upper plate faults on the subduction margin of northern Chile. *Scientific Reports*, *11*(1), 21444. https://doi.org/10.1038/s41598-021-00875-6

González, G., Salazar, P., Loveless, J. P., Allmendinger, R. W., Aron, F., & Shrivastava, M. (2015). Upper plate reverse fault reactivation and the unclamping of the megathrust during the 2014 northern Chile earthquake sequence. *Geology*, *43*(8), 671–674. https://doi.org/10.1130/G36703.1

Habel, T., Simoes, M., Lacassin, R., Carrizo, D., & Aguilar, G. (2023). A contribution to the quantification of crustal shortening and kinematics of deformation across the Western Andes (g∼20-22° S). *Solid Earth*, *14*(1), 17–42. https://doi.org/10.5194/SE-14-17-2023

Hartley, A. J., Mather, A. E., Jolley, E., & Turner, P. (2005). Climatic controls an alluvial-fan activity, Coastal Cordillera, northern Chile. *Geological Society - Special Publications*, *251*(1), 95–116. https://doi.org/10.1144/GSL.SP.2005.251.01.08

Herrera, C., Cassidy, J. F., Dosso, S. E., Dettmer, J., Bloch, W., Sippl, C., & Salazar, P. (2021). The crustal stress field inferred from focal mechanisms in northern Chile. *Geophysical Research Letters*, *48*(8), e2021GL092889. https://doi.org/10.1029/2021GL092889

Hoke, G. D., Isacks, B. L., Jordan, T. E., Blanco, N., Tomlinson, A. J., & Ramezani, J. (2007). Geomorphic evidence for post-10 Ma uplift of the western flank of the central Andes 18°30′-22°S. *Tectonics*, *26*(5). https://doi.org/10.1029/2006TC002082

Hoke, G. D., Isacks, B. L., Jordan, T. E., & Yu, J. S. (2004). Groundwater-sapping origin for the giant quebradas of northern Chile. *Geology*, *32*(7), 605. https://doi.org/10.1130/G20601.1

Holbrook, J., & Schumm, S. A. (1999). Geomorphic and sedimentary response of rivers to tectonic deformation: A brief review and critique of a tool for recognizing subtle epeirogenic deformation in modern and ancient settings. *Tectonophysics*, *305*(1–3), 287–306. https://doi.org/10.1016/S0040-1951(99)00011-6

Houston, J., & Hartley, A. J. (2003). The central Andean west-slope rainshadow and its potential contribution to the origin of hyper-aridity in the Atacama Desert. *International Journal of Climatology*, *23*(12), 1453–1464. https://doi.org/10.1002/joc.938

Humphrey, N. F., & Konrad, S. K. (2000). River incision or diversion in response to bedrock uplift | Geology | GeoScienceWorld. *Geology*, *28*(1), 43–46. https://doi.org/10.1130/0091-7613(2000)028<0043:riodir>2.3.co;2

Ishiyama, T., Sato, H., Kato, N., Nakayama, T., & Abe, S. (2013). Active blind thrusts beneath the Tokyo metropolitan area: Seismic hazards and inversion tectonics. *Geophysical Research Letters*, *40*(11), 2608–2612. https://doi.org/10.1002/grl.50487

Jordan, T. E., Kirk-Lawlor, N. E., Blanco, N. P., Rech, J. A., & Cosentino, N. J. (2014). Landscape modification in response to repeated onset of hyperarid paleoclimate states since 14 Ma, Atacama Desert, Chile. *Geological Society of America Bulletin*, *126*(7–8), 1016–1046. https://doi.org/10.1130/B30978.1

Jordan, T. E., Nester, P. L., Blanco, N., Hoke, G. D., Dávila, F., & Tomlinson, A. J. (2010). Uplift of the Altiplano-Puna plateau: A view from the west. *Tectonics*, *29*(5). https://doi.org/10.1029/2010TC002661

Jungers, M. C., Heimsath, A. M., Amundson, R., Balco, G., Shuster, D., & Chong, G. (2013). Active erosion–deposition cycles in the hyperarid Atacama Desert of Northern Chile. *Earth and Planetary Science Letters*, *371–372*, 125–133. https://doi.org/10.1016/J.EPSL.2013.04.005

Karger, D., Conrad, O., Böhner, J., Kawohl, T., Kreft, H., Soria-Auza, R., et al. (2018). Data from: Climatologies at high resolution for the earth's land surface areas. https://doi.org/10.5061/dryad.kd1d4

Karger, D., Conrad, O., Böhner, J., Kawohl, T., Kreft, H., Soria-Auza, R. W., et al. (2017). Climatologies at high resolution for the earth's land surface areas. *Scientific Data*, *4*(1), 1–20. https://doi.org/10.1038/sdata.2017.122

Kaveh-Firouz, A., Burg, J. P., & Giachetta, E. (2024). Landscape evolution in orogenic plateaus: Insights from quantitative morphotectonic analysis of the Turkish–Iranian Plateau and Caucasus regions. *Earth Surface Processes and Landforms*, *49*(3), 1214–1238. https://doi.org/10.1002/ESP.5756

Kaveh-Firouz, A., Burg, J. P., Haghipour, N., Mandal, S. K., Christl, M., & Mohammadi, A. (2023). Tectonics, base-level fluctuations, and climate impact on the Eocene to present-day erosional pattern of the Arabia-Eurasia collision zone (NNW Iranian plateau and West Alborz mountains). *Tectonics*, *42*(8), e2022TC007684. https://doi.org/10.1029/2022TC007684

Keefer, D. K., & Moseley, M. E. (2004). Southern Peru desert shattered by the great 2001 earthquake: Implications for paleoseismic and paleo-El Niño–Southern Oscillation records. *Proceedings of the National Academy of Sciences*, *101*(30), 10878–10883. https://doi.org/10.1073/pnas.0404320101

Kirby, E., & Whipple, K. X. (2012). Expression of active tectonics in erosional landscapes. *Journal of Structural Geology*, *44*, 54–75. https://doi.org/10.1016/j.jsg.2012.07.009

Kirk-Lawlor, N. E., Jordan, T. E., Rech, J. A., & Lehmann, S. B. (2013). Late Miocene to early Pliocene paleohydrology and landscape evolution of northern Chile, 19° to 20° S. *Palaeogeography, Palaeoclimatology, Palaeoecology*, *387*, 76–90. https://doi.org/10.1016/j.palaeo.2013.07.011

Klinger, Y., Xu, X., Tapponnier, P., Van der Woerd, J., Lasserre, C., & King, G. (2005). High-resolution satellite imagery mapping of the surface rupture and slip distribution of the Mw ∼7.8, 14 November 2001 Kokoxili earthquake, Kunlun fault, northern tibet, China. *Bulletin of the Seismological Society of America*, *95*(5), 1970–1987. https://doi.org/10.1785/0120040233

Kober, F., Ivy-Ochs, S., Schlunegger, F., Baur, H., Kubik, P. W., & Wieler, R. (2007). Denudation rates and a topography-driven rainfall threshold in northern Chile: Multiple cosmogenic nuclide data and sediment yield budgets. *Geomorphology*, *83*(1–2), 97–120. https://doi.org/10.1016/j.geomorph.2006.06.029

Kondo, H., Toda, S., Okumura, K., Takada, K., & Chiba, T. (2008). A fault scarp in an urban area identified by LiDAR survey: A case study on the Itoigawa–Shizuoka tectonic line, central Japan. *Geomorphology*, *101*(4), 731–739. https://doi.org/10.1016/J.GEOMORPH.2008.02.012

Krüger, F., Kulikova, G., & Landgraf, A. (2017). Instrumental magnitude constraints for the 11 July 1889, Chilik earthquake. *Geological Society - Special Publications*, *432*(1), 41–72. https://doi.org/10.1144/SP432.8/ASSET/34D2CE94-AD1D-46F1-A368-49ADC1B50C57/ASSETS/GRAPHIC/SP432-1489EQ07.JPEG

Landgraf, A., KüBler, S., Hintersberger, E., & Stein, S. (2017). Active tectonics, earthquakes and palaeoseismicity in slowly deforming continents. *Geological Society - Special Publications*, *432*(1), 1–12. https://doi.org/10.1144/SP432.13

Legrand, D., Delouis, B., Dorbath, L., David, C., Campos, J., Marquéz, L., et al. (2007). Source parameters of the Mw=6.3 Aroma crustal earthquake of July 24, 2001 (northern Chile), and its aftershock sequence. *Journal of South American Earth Sciences*, *24*(1), 58–68. https://doi.org/10.1016/j.jsames.2007.02.004

Leonard, J. S., Whipple, K. X., & Heimsath, A. M. (2024). Controls on topography and erosion of the north-central Andes. *Geology*, *52*(2), 153–158. https://doi.org/10.1130/G51618.1

Lettis, W. R., Wells, D. L., & Baldwin, J. N. (1997). Empirical observations regarding reverse earthquakes, blind thrust faults, and quaternary deformation: Are blind thrust faults truly blind? *Bulletin of the Seismological Society of America*, *87*(5), 1171–1198. https://doi.org/10.1785/BSSA0870051171

Loveless, J. P., Allmendinger, R. W., Pritchard, M. E., Garroway, J. L., & González, G. (2009). Surface cracks record long-term seismic segmentation of the Andean margin. *Geology*, *37*(1), 23–26. https://doi.org/10.1130/G25170A.1

Loveless, J. P., Hoke, G. D., Allmendinger, R. W., González, G., Isacks, B. L., & Carrizo, D. A. (2005). Pervasive cracking of the northern Chilean Coastal Cordillera: New evidence for forearc extension. *Geology*, *33*(12), 973–976. https://doi.org/10.1130/G22004.1

Madella, A., Delunel, R., Audin, L., & Schlunegger, F. (2018). Why is there no coastal Cordillera at the Arica Bend (western central Andes)? *Basin Research*, *30*(S1), 248–268. https://doi.org/10.1111/bre.12218

Maesano, F. E., D'Ambrogi, C., Burrato, P., & Toscani, G. (2015). Slip-rates of blind thrusts in slow deforming areas: Examples from the Po Plain (Italy). *Tectonophysics*, *643*, 8–25. https://doi.org/10.1016/j.tecto.2014.12.007

Maldonado, V., Contreras, M., & Melnick, D. (2021). A comprehensive database of active and potentially-active continental faults in Chile at 1: 25,000 scale. *Scientific Data*, *8*(1), 20. https://doi.org/10.1038/s41597-021-00802-4

Martínez, F., Fuentes, G., Perroud, S., & Bascuñan, S. (2021). Buried thrust belt front of the western Central Andes of northern Chile: Style, age, and relationship with basement heterogeneities. *Journal of Structural Geology*, *147*, 104337. https://doi.org/10.1016/j.jsg.2021.104337

McMichael, C., Dasgupta, S., Ayeb-Karlsson, S., Hasna Zainurin Ku Zainol Abidin, K., Adib Mohammad Razi, M., Mohd Bukari, S., et al. (2022). A 30 m global map of elevation with forests and buildings removed. *Environmental Research Letters*, *17*(2), 024016. https://doi.org/10.1088/1748-9326/AC4D4F

Medina-Cascales, I., García-Tortosa, F. J., Martin-Rojas, I., Pérez-Peña, J. V., & Alfaro, P. (2021). Tectonic geomorphology of an active slow-moving, intrabasinal fault: The Galera Fault (Guadix-Baza Basin, central Betic Cordillera, southern Spain). *Geomorphology*, *393*, 107941. https://doi.org/10.1016/J.GEOMORPH.2021.107941

Merritts, D., & Vincent, K. R. (1989). Geomorphic response of coastal streams to low, intermediate, and high rates of uplift, Mendocino triple junction region, northern California. *Geological Society of America Bulletin*, *101*(11), 1373–1388. https://doi.org/10.1130/0016-7606(1989)101<1373:GROCST>2.3.CO;2

Midland Valley. (2014). FieldMove Clino iPhone user guide.

Mittelstädt, J., & Victor, P. (2020). Active fault database for the Atacama Fault System (N-Chile) as basis for tracking forearc segmentation [Dataset]. *GFZ Data Services*. https://doi.org/10.5880/GFZ.4.1.2020.012

Morandé, J., Gallardo, F., & Farías, M. (2015). Carta Guaviña, Región de Tarapacá. *Servicio Nacional de Geología y Minería, Carta Geológica de Chile, Serie Geología Básica*, *177*(1).

Mortimer, C. (1980). Drainage evolution in the Atacama Desert of northernmost Chile. *Andean Geology*, *11*, 3–28.

Mortimer, C., Farrar, E., & Saric, N. (1974). K-Ar ages from Tertiary lavas of the northernmost Chilean Andes. *Geologische Rundschau*, *63*(2), 484–490. https://doi.org/10.1007/BF01820825

Mortimer, C., & Rendic, N. S. (1975). Cenozoic studies in northernmost Chile. *Geologische Rundschau*, *64*(1), 395–420. https://doi.org/10.1007/BF01820676

Muñoz, N., & Charrier, R. (1996). Uplift of the western border of the Altiplano on a west-vergent thrust system, Northern Chile. *Journal of South American Earth Sciences*, *9*(3–4), 171–181. https://doi.org/10.1016/0895-9811(96)00004-1

Muñoz-Farías, S., Ritter, B., Dunai, T. J., Morales-Leal, J., Campos, E., Spikings, R., & Riquelme, R. (2023). Geomorphological significance of the Atacama Pediplain as a marker for the climatic and tectonic evolution of the Andean forearc, between 26° to 28°S. *Geomorphology*, *420*, 108504. https://doi.org/10.1016/J.GEOMORPH.2022.108504

Naranjo, J., & Paskoff, R. (1985). Evolución cenozoica del piedemonte andino en la Pampa del Tamarugal, norte de Chile (18–21 S). *4th Congreso Geológico Chileno*, 149–185.

Nazari, H., Ritz, J. F., Walker, R. T., Salamati, R., Rizza, M., Patnaik, R., et al. (2014). Palaeoseismic evidence for a medieval earthquake, and preliminary estimate of late Pleistocene slip-rate, on the Firouzkuh strike-slip fault in the Central Alborz region of Iran. *Journal of Asian Earth Sciences*, *82*, 124–135. https://doi.org/10.1016/J.JSEAES.2013.12.018

Nester, P., & Jordan, T. (2012). The Pampa del Tamarugal Forearc Basin in Northern Chile: The Interaction of Tectonics and Climate. *Tectonics of Sedimentary Basins: Recent Advances*, 369–381. https://doi.org/10.1002/9781444347166.CH18

Nicol, A., Khajavi, N., Pettinga, J. R., Fenton, C., Stahl, T., Bannister, S., et al. (2018). Preliminary geometry, displacement, and kinematics of fault ruptures in the epicentral region of the 2016 Mw 7.8 Kaikōura, New Zealand, earthquake. *Bulletin of the Seismological Society of America*, *108*(3B), 1521–1539. https://doi.org/10.1785/0120170329

Niemeyer, H. R., Niemeyer, H. F., & Schiappacasse, V. (1984). Una falla geolofica sub-actual detectada en el sitio arqueologico 14. desembocadura del río Camarones-Desierto de Atacama, Chile. *Revista Geologica de Chile*, *0*(22). Retrieved from http://www.andeangeology.cl/index.php/revista1/article/view/V11n2-a08

Nishiizumi, K., Caffee, M. W., Finkel, R. C., Brimhall, G., & Mote, T. (2005). Remnants of a fossil alluvial fan landscape of Miocene age in the Atacama Desert of northern Chile using cosmogenic nuclide exposure age dating. *Earth and Planetary Science Letters*, *237*(3–4), 499–507. https://doi.org/10.1016/j.epsl.2005.05.032

Norabuena, E., Leffler-Griffin, L., Mao, A., Dixon, T., Stein, S., Sacks, I. S., et al. (1998). Space geodetic observations of Nazca-South America convergence across the central Andes. *Science*, *279*(5349), 358–362. https://doi.org/10.1126/science.279.5349.358

Norton, K., & Schlunegger, F. (2011). Migrating deformation in the Central Andes from enhanced orographic rainfall. *Nature Communications*, *2*(1), 1–7. https://doi.org/10.1038/ncomms1590

Oskin, M. E., Le, K., & Strane, M. D. (2007). Quantifying fault-zone activity in arid environments with high-resolution topography. *Geophysical Research Letters*, *34*, 23–28. https://doi.org/10.1029/2007GL031295

Pedrera, A., Pérez-Peña, J. V., Galindo-Zaldívar, J., Azañón, J. M., & Azor, A. (2009). Testing the sensitivity of geomorphic indices in areas of low-rate active folding (eastern Betic Cordillera, Spain). *Geomorphology*, *105*(3–4), 218–231. https://doi.org/10.1016/J.GEOMORPH.2008.09.026

Pérez-Peña, J. V., Azor, A., Azañón, J. M., & Keller, E. A. (2010). Active tectonics in the Sierra Nevada (Betic Cordillera, SE Spain): Insights from geomorphic indexes and drainage pattern analysis. *Geomorphology*, *119*(1–2), 74–87. https://doi.org/10.1016/J.GEOMORPH.2010.02.020

Peri, V. G., Haghipour, N., Christl, M., Terrizzano, C., Kaveh-Firouz, A., Leiva, M. F., et al. (2022). Quaternary landscape evolution in the Western Argentine Precordillera constrained by 10Be cosmogenic dating. *Geomorphology*, *396*, 107984. https://doi.org/10.1016/J.GEOMORPH.2021.107984

Pinto, L., Hérail, G., & Charrier, R. (2004). Sedimentación sintectónica asociada a las estructuras neógenas en la Precordillera de la zona de Moquella, Tarapacá (19°15'S, norte de Chile). *Revista Geologica de Chile*, *31*(1). https://doi.org/10.4067/S0716-02082004000100002

Pinto, L., Hérail, G., Sepúlveda, S. A., & Krop, P. (2008). A Neogene giant landslide in Tarapacá, northern Chile: A signal of instability of the westernmost Altiplano and palaeoseismicity effects. *Geomorphology*, *102*(3–4), 532–541. https://doi.org/10.1016/j.geomorph.2008.05.044

Placzek, C., Granger, D. E., Matmon, A., Quade, J., & Ryb, U. (2014). Geomorphic process rates in the central Atacama Desert, Chile: Insights from cosmogenic nuclides and implications for the onset of hyperaridity. *American Journal of Science*, *314*(10), 1462–1512. https://doi.org/10.2475/10.2014.03

Reutter, K. J., Scheuber, E., & Chong, G. (1996). The precordilleran fault system of Chuquicamata, northern Chile: Evidence for reversals along arc-parallel strike-slip faults. *Tectonophysics*, *259*(1–3), 213–228. https://doi.org/10.1016/0040-1951(95)00109-3

Reutter, K. J., Scheuber, E., & Helmcke, D. (1991). Structural evidence of orogen-parallel strike slip displacements in the Precordillera of northern Chile. *Geologische Rundschau*, *80*(1), 135–153. https://doi.org/10.1007/BF01828772/METRICS

Riesner, M., Lacassin, R., Simoes, M., Armijo, R., Rauld, R., & Vargas, G. (2017). Kinematics of the active West Andean fold-and-thrust belt (central Chile): Structure and long-term shortening rate. *Tectonics*, *36*(2), 287–303. https://doi.org/10.1002/2016TC004269

Riesner, M., Lacassin, R., Simoes, M., Carrizo, D., & Armijo, R. (2018). Revisiting the crustal structure and kinematics of the central Andes at 33.5°S: Implications for the mechanics of Andean mountain building. *Tectonics*, *37*(5), 1347–1375. https://doi.org/10.1002/2017TC004513

Ritter, B., Diederich-Leicher, J. L., Binnie, S. A., Stuart, F. M., Wennrich, V., Bolten, A., & Dunai, T. J. (2022). Impact of CaSO4-rich soil on Miocene surface preservation and Quaternary sinuous to meandering channel forms in the hyperarid Atacama Desert. *Scientific Reports*, *12*(1), 1–9. https://doi.org/10.1038/s41598-022-22787-9

Ritter, B., Stuart, F. M., Binnie, S. A., Gerdes, A., Wennrich, V., & Dunai, T. J. (2018). Neogene fluvial landscape evolution in the hyperarid core of the Atacama Desert. *Scientific Reports*, *8*(1), 13952. https://doi.org/10.1038/s41598-018-32339-9

Salazar, P., Kummerow, J., Wigger, P., Shapiro, S., & Asch, G. (2017). State of stress and crustal fluid migration related to west-dipping structures in the slab-forearc system in the northern Chilean subduction zone. *Geophysical Journal International*, *208*(3), 1403–1413. https://doi.org/10.1093/gji/ggw463

Santibáñez, I., Cembrano, J., García-Pérez, T., Costa, C., Yáñez, G., Marquardt, C., et al. (2019). Crustal faults in the Chilean Andes: Geological constraints and seismic potential. *Redalyc.Org*, *46*(1), 32. https://doi.org/10.5027/andgeov46n1-3067

Scheuber, E., & Reutter, K.-J. (1992). Magmatic arc tectonics in the central Andes between 21° and 25°S. *Tectonophysics*, *205*(1–3), 127–140. https://doi.org/10.1016/0040-1951(92)90422-3

Schildgen, T. F., Hodges, K. V., Whipple, K. X., Pringle, M. S., Van Soest, M., & Cornell, K. (2009). Late Cenozoic structural and tectonic development of the western margin of the central Andean Plateau in southwest Peru. *Tectonics*, *28*(4). https://doi.org/10.1029/2008TC002403

Schildgen, T. F., Hodges, K. V., Whipple, K. X., Reiners, P. W., & Pringle, M. S. (2007). Uplift of the western margin of the Andean plateau revealed from canyon incision history, southern Peru. *Geology*, *35*(6), 523. https://doi.org/10.1130/G23532A.1

Schreurs, G., & Colletta, B. (1998). Analogue modelling of faulting in zones of continental transpression and transtension. *Geological Society - Special Publications*, *135*(1), 59–79. https://doi.org/10.1144/GSL.SP.1998.135.01.05

Schwanghart, W., & Scherler, D. (2014). Short communication: TopoToolbox 2-MATLAB-based software for topographic analysis and modeling in earth surface sciences. *Earth Surface Dynamics*, *2*, 1–7. https://doi.org/10.5194/esurf-2-1-2014

Schwanghart, W., & Scherler, D. (2017). Bumps in river profiles: Uncertainty assessment and smoothing using quantile regression techniques. *Earth Surface Dynamics*, *5*(4), 821–839. https://doi.org/10.5194/esurf-5-821-2017

Sillitoe, R. H., & McKee, E. H. (1996). Age of supergene oxidation and enrichment in the Chilean porphyry copper province. *Economic Geology*, *91*(1), 164–179. https://doi.org/10.2113/gsecongeo.91.1.164

Sippl, C., Schurr, B., Münchmeyer, J., Barrientos, S., & Oncken, O. (2023). The Northern Chile forearc constrained by 15 years of permanent seismic monitoring. *Journal of South American Earth Sciences*, *126*, 104326. https://doi.org/10.1016/J.JSAMES.2023.104326

Somoza, R. (1998). Updated azca (Farallon)—South America relative motions during the last 40 My: Implications for mountain building in the central Andean region. *Journal of South American Earth Sciences*, *11*(3), 211–215. https://doi.org/10.1016/s0895-9811(98)00012-1

Thouret, J. C., Wörner, G., Gunnell, Y., Singer, B., Zhang, X., & Souriot, T. (2007). Geochronologic and stratigraphic constraints on canyon incision and Miocene uplift of the Central Andes in Peru. *Earth and Planetary Science Letters*, *263*(3–4), 151–166. https://doi.org/10.1016/J.EPSL.2007.07.023

Tindall, S. E., & Davis, G. H. (1999). Monocline development by oblique-slip fault-propagation folding: The east Kaibab monocline, Colorado plateau, Utah. *Journal of Structural Geology*, *21*(10), 1303–1320. https://doi.org/10.1016/S0191-8141(99)00089-9

Valenzuela, I., Herrera, S., Pinto, L., & Real, I. (2014). Carta Camiña, regiones de Arica y Parinacota y de Tarapacá. Servicio Nacional de Geología y Minería, Carta Geológica de Chile, Serie Geología Básica, 170.

van der Wal, J. L. N., Nottebaum, V. C., Stauch, G., Binnie, S. A., Batkhishig, O., Lehmkuhl, F., & Reicherter, K. (2021). Geomorphological evidence of active faulting in low seismicity regions—Examples from the valley of Gobi Lakes, southern Mongolia. *Frontiers in Earth Science*, *8*, 589814. https://doi.org/10.3389/FEART.2020.589814

Vega-Ruiz, A., Victor, P., & Steinritz, V. (2024). Fault database of the Northern Chile forearc between 18°50′S and 19°45′S [Dataset]. *GFZ Data Services*. https://doi.org/10.5880/GFZ.4.1.2023.007

Victor, P., Oncken, O., & Glodny, J. (2004). Uplift of the western Altiplano plateau: Evidence from the Precordillera between 20° and 21°S (northern Chile). *Tectonics*, *23*(4). https://doi.org/10.1029/2003TC001519

Wang, F., Michalski, G., Seo, J. H., Granger, D. E., Lifton, N., & Caffee, M. (2015). Beryllium-10 concentrations in the hyper-arid soils in the Atacama Desert, Chile: Implications for arid soil formation rates and El Niño driven changes in Pliocene precipitation. *Geochimica et Cosmochimica Acta*, *160*, 227–242. https://doi.org/10.1016/J.GCA.2015.03.008

Wang, Y., Zhang, B., Hou, J., & Xu, X. (2014). Structure and tectonic geomorphology of the Qujiang fault at the intersection of the Ailao Shan–Red River fault and the Xianshuihe–Xiaojiang fault system, China. *Tectonophysics*, *634*, 156–170. https://doi.org/10.1016/J.TECTO.2014.07.031

Wennrich, V., Böhm, C., Brill, D., Carballeira, R., Hoffmeister, D., Jaeschke, A., et al. (2024). Late Pleistocene to modern precipitation changes at the Paranal clay pan, central Atacama Desert. *Global and Planetary Change*, *233*, 104349. https://doi.org/10.1016/J.GLOPLACHA.2023.104349

Whitney, B. B., & Hengesh, J. V. (2015). Geomorphological evidence of neotectonic deformation in the Carnarvon basin, western Australia. *Geomorphology*, *228*, 579–596. https://doi.org/10.1016/J.GEOMORPH.2014.10.020

Whittaker, A. C. (2012). How do landscapes record tectonics and climate? *Lithosphere*, *4*(2), 160–164. https://doi.org/10.1130/RF.L003.1

Wobus, C., Whipple, K. X., Kirby, E., Snyder, N., Johnson, J., Spyropolou, K., et al. (2006). Tectonics from topography: Procedures, promise, and pitfalls. In *Tectonics, climate, and landscape evolution*. Geological Society of America. https://doi.org/10.1130/2006.2398(04

Yang, H. (2015). Recent advances in imaging crustal fault zones: A review. *Earthquake Science*, *28*(2), 151–162. https://doi.org/10.1007/S11589-015-0114-3

Yang, X., Li, W., & Qin, Z. (2015). Calculation of reverse-fault-related parameters using topographic profiles and fault bedding. *Geodesy and Geodynamics*, *6*(2), 106–112. https://doi.org/10.1016/J.GEOG.2014.09.002

Zachos, J., Pagani, H., Sloan, L., Thomas, E., & Billups, K. (2001). Trends, rhythms, and aberrations in global climate 65 Ma to present. *Science*, *292*(5517), 686–693. https://doi.org/10.1126/SCIENCE.1059412/SUPPL_FILE/INDEX.HTML

Zhang, P. Z. (2013). Beware of slowly slipping faults. *Nature Geoscience*, *6*(5), 323–324. https://doi.org/10.1038/ngeo1811

Zielke, O., & Arrowsmith, J. R. (2012). LaDiCaoz and LiDARimager—MATLAB GUIs for LiDAR data handling and lateral displacement measurement. *Geosphere*, *8*(1), 206–221. https://doi.org/10.1130/GES00686.1